ANISOTROPIES OF ULTRATHIN Co/W(110) AND CoO/Co/W(110) FILMS

IN-PLANE ANISOTROPY OF ULTRATHIN Co/W(110) FILMS AND THE NÉEL TRANSITION IN BILAYER ULTRATHIN CoO/Co/W(110) FILMS

by

ANDREW BARTLETT, B.Sc. (Hons.)

A Thesis Submitted to the
School of Graduate Studies
in Partial Fulfilment of the
Requirements for the Degree of
Master of Science

McMaster University

Hamilton Ontario

MASTER OF SCIENCE (2012)
Department of Physics & Astronomy
McMaster University, Hamilton, Ontario

TITLE: In-Plane Anisotropy of Ultrathin Co/W(110) Films and the Néel Transition in Bilayer Ultrathin CoO/Co/W(110) Films
AUTHOR: Andrew Bartlett, B.Sc. (Hons.), Memorial University
SUPERVISOR: Dr. David Venus
NUMBER OF PAGES: xvii, 128

Abstract

The study of ultrathin magnetic films offers novel magnetic phenomena due to the reduced symmetry of these two dimensional (2D) systems. The magnetic anisotropy differentiates behaviour in ultrathin films from the bulk environment, as additional anisotropies emerge from the ultrathin film thickness and the inherent strain of ultrathin films. In this work, the in-plane magnetic anisotropy of strained ferromagnetic (FM) ultrathin Co(0001) films grown on a W(110) substrate is measured over a range of temperatures (150-320 K). Low energy electron diffraction (LEED) and Auger electron spectroscopy (AES) were used to determine the film structure and thickness. The anisotropy is derived from the quotient of the saturation magnetization and the transverse susceptibility, which are measured using the surface magneto-optic Kerr effect (SMOKE). The results are comparable to estimates by Fritzsche *et. al* [1].

This work's second objective is to study the Néel transition in antiferromagnetic (AFM) ultrathin films. The zero net magnetization of AFM materials and the minute sample size of ultrathin films make magnetic measurements impossible with conventional methods. Progress has been made using a three dimensional (3D) stack of many such films, although stacking films complicates the magnetic anisotropy. An alternative approach is to study a single AFM ultrathin film that is coupled by the interfacial exchange interaction to a FM ultrathin film. The interfacial exchange interaction is an anisotropy of AFM/FM bilayers that causes a change in the in-plane transverse magnetic susceptibility as the temperature passes through the Néel point. The upper layers of ultrathin Co/W(110) films were oxidized to produce ultrathin CoO/Co/W(110) films, creating an AFM/FM bilayer system. SMOKE measurement of the transverse magnetic susceptibility of the FM Co layer reveal the Néel transition of the AFM layer indirectly through the interfacial exchange interaction.

Acknowledgements

I am grateful for the teaching, supervision, and support of Dr. David Venus. Technical assistance provided by Marek Kiela was essential to the completion of this project. Rob D'Ortenzio, Peter Nguyen, and Katharina Fritsch trained me in the many technical procedures required to perform my experiments. I appreciate the companionship of Mohdeep Singh, Peter Nguyen, and Randy Belanger in the lab. I am thankful to the McMaster Physics & Astronomy Department for providing a friendly and productive learning environment. I am grateful for the funding I received from the National Science and Engineering Research Council, the Government of Ontario, McMaster University, and the afore mentioned Physics & Astronomy Department.

This project would not be possible without my loving fiancée, Claire Woodworth, who motivated me to work around the clock and who has been of great assistance in editing this manuscript. Likewise, I would like to thank my parents and brothers for their unwavering encouragement and support throughout my entire education.

Contents

List of Tables

List of Figures

List of Abbreviations

- a - Lattice parameter
- ac - Alternating Current
- AES - Auger Electron Spectroscopy
- AFM - Antiferromagnetic
- ap - Aperture
- Atm - Atmospheric pressure
- $\mathbf{B}$ - Magnetic field
- $\mathbf{b}$ - Reciprocal lattice parameter
- bcc - Body Centred Cubic
- BLS - Brillouin Light Scattering
- CCD - Charge Coupled Device
- d - Inter-planar spacing
- E - Energy
- $\mathbf{E}$ - Electric field
- f - Energy density
- fcc - Face Centred Cubic
- FM - Ferromagnetic
- FMR - Ferromagnetic Resonance
- FvdM - Frank-van der Merwe
- $\mathbf{G}$ - Reciprocal lattice vector
- $\mathbf{H}$ - Applied field
- $\mathcal{H}$ - Hamiltonian
- h - Planck's constant
- HC - High Current
- hcp - Hexagonal Closed Packed
- HV - High Voltage
- I - Laser intensity
- i - Imaginary unit
- IC - Ion Current

- Im - Imaginary component of a complex number
- J - Exchange coupling constant
- K - Anisotropy constant
- $\mathbf{k}$ - Wave vector
- $\mathbf{L}$ - Orbital momentum
- LEED - Low Energy Electron Diffraction
- $\mathbf{M}$ - Magnetization
- $\mathbf{m}$ - Magnetic moment
- $\mathbf{m}_e$ - Electron mass
- $\mathbf{M}_s$ - Saturation magnetization
- ML - Monolayer
- MOKE - Magneto-Optic Kerr Effect
- MR - Magnetoresistance
- $\hat{\mathbf{n}}$ - Surface normal unit vector
- N - Complex index of refraction
- $\overleftrightarrow{N}$ - Demagnetization tensor
- n - Diffraction order
- PD - Photodetector
- ps - Pseudomorphic
- Q - Voigt parameter
- R - Jones reflection matrix
- $\mathbf{r}$ - Displacement vector
- Re - Real component of a complex number
- RF - Radio Frequency
- $\mathbf{S}$ - Spin angular momentum
- SEMPA - Scanning Electron Microscopy with Polarization Analysis
- SK - Stranski-Krastanov
- SMOKE - Surface Magneto-Optic Kerr Effect

- SPLEEM - Spin-Polarized Low-Energy Electron Microscopy
- SQUID - Superconducting Quantum Interference Device
- STM - Scanning Tunnelling Microscopy
- STS - Scanning Tunnelling Spectroscopy
- t - Thickness
- T_C - Curie temperature
- T-MOKE - Transvers Magneto-Optic Kerr Effect
- T_N - Néel temperature
- TOM - Torsion Oscillation Magnetometry
- TSP - Titanium Sublimation Pump
- UHV - Ultrahigh Vacuum
- V - Volume
- VW - Volmer-Weber
- 2D - Two Dimensional
- 3D - Three Dimensional
- γ - Elastic modulus
- ϵ - Extinction ratio
- ε - Strain
- η - lattice mistmatch
- Θ - Kerr rotation per saturated monolayer
- λ - Wavelength
- λ_m - Constant
- λ_o - Magnetostriction constant
- μ_B - Bohr magneton
- σ - Stress
- σ_E - Energy variance
- σ_{tot} - Surface energy density
- Φ - Kerr rotation
- χ - Magnetic susceptibility
- Ω - Constant

Declaration of Academic Achievement

I performed all of the experimental work including sample growth, experimental measurements, and analysis.

Chapter 1

Introduction

1.1 Ultrathin magnetic films

Ultrathin magnetic films are true two dimensional (2D) systems that display novel phenomena and provide a necessary test for magnetic theories at low dimensionality [2]. Ultrathin films have thicknesses less than that of a magnetic domain, on the order of 0.1 to 10 monolayers (ML) of atoms. Exotic magnetic behaviours arise from ultrathin magnetic films because the high surface to volume ratio brings about the importance of surface phenomena. Magnetism in condensed matter systems is based on the interaction of neighbouring atoms; therefore, the atomic neighbourhood, which differs for bulk and surface atoms, dictates the magnetic properties of a sample. As ultrathin films lack structural integrity to withstand small vibrations, they must be grown on a substrate, the atoms of which constitute the atomic neighbourhood of the film's surface atoms. The opposite surface may have a completely different neighbourhood, be it vacuum, gas, or another film. The substrate is a plane of a single crystal, in the case of this work a tungsten (110) surface (W (110) surface), with few defects. Besides altering the atomic neighbourhood of the surface atoms, the substrate affects the atomic neighbourhood within the film by influencing the crystal structure of the film, as it is the template for film growth. Ultrathin magnetic films are an exciting field of research that provides new information on complex magnetic interactions that are essential to the development of magnetic data storage devices and the blossoming field of spintronics.

1.2 Magnetic anisotropy of ultrathin films

The magnetic properties of a crystal are extremely sensitive to the spatial properties of the lattice. Lattices are made up of discrete regularly spaced points, making the crystalline environment intrinsically anisotropic. This gives rise to the magnetic anisotropy, which is the directional dependence of the magnetization of atoms arranged on a crystal lattice. The magnetization of the crystal has a preferred direction, called the easy axis, that is dependent on the symmetries of the crystal lattice.

The total magnetic anisotropy is composed of three parts:

- **Magnetocrystalline anisotropy** is the directional dependence of the magnetization due to the symmetries of the lattice.

- **Shape anisotropy** is the directional dependence of the magnetization due to the shape, or boundary of the crystal, which affects the direction of magnetization through demagnetization fields.
- **Magnetoelastic anisotropy** is the directional dependence of the magnetization due to strain changing the symmetries of the lattice.

The shape and magnetoelastic anisotropies are secondary to the magnetocrystalline anisotropy in bulk materials where there are no surfaces; however, in ultrathin films the relative importance of each contribution can be tuned by varying characteristics of the film such as the thickness, the substrate on which the film is grown, and the temperature. This opens a door to new magnetic phenomena. A further discussion of anisotropies will be presented in the next chapter.

Ultrathin magnetic films must be kept in an ultrahigh vacuum (UHV) chamber or be capped by a nonmagnetic layer to protect the delicate films from the environment. A capping layer significantly changes the spatial crystalline structure of a film, compromising its magnetic anisotropy [3, 4]. This is called an *ex situ* measurement. To study the magnetic properties of a film in its most basic form, it must be grown and analyzed in UHV conditions, that is, *in situ*.

One of the main goals of this work is to measure the magnetic anisotropy of Co ultrathin films grown on a W (110) substrate *in situ*. In order to do this, Co ultrathin films will be examined by the surface magneto-optic Kerr effect (SMOKE). This method allows *in situ* magnetic measurements within the surface plane (longitudinal and transverse) and out of the surface plane. SMOKE detects the magnetization of the sample through the coupling of the electron spins of the sample to the polarization of a reflected laser beam. The rotation of the plane of linear polarization is measured using crossed polarizers. The sample size needed for SMOKE measurements is on the scale of microns to a millimetre squared, depending on whether the beam is focused on the sample or collimated. In this work a collimated beam is used because the sample is large (~ 1 cm^2). The main disadvantage of this method is that the magnetic information obtained is not absolute but must be calibrated.

There are other measurement techniques that have the sensitivity to quantify the magnetic anisotropy of ultrathin films. Superconducting quantum interference device (SQUID) magnetometry, magnetoresistance (MR) [5], and ferromagnetic resonance measurements (FMR) [6] sample the entire crystal and thus require uniformity across a large area. These methods have inherent technical difficulties when implementing *in situ* measurements; therefore, *ex situ* measurements are favoured. MR measurements are obscured by a direct dependence on impurities in the sample, interface roughness, and temperature [5]. SQUID magnetometry is extremely sensitive, but must be performed at low temperatures that require the sample be placed in a cryostat. Brillouin light scattering (BLS) can be implemented *in situ* and requires relatively small sample sizes [7]. BLS and FMR are powerful techniques for measuring dynamic magnetic processes [5], although magnetic anisotropies must be inferred by examining resonance frequencies of spin waves. These methods require large applied fields that are difficult to achieve *in situ*. Scanning electron microscopy with polarization analysis (SEMPA) provides *in situ* images that directly measure the magnetization vector [5]. SEMPA does not allow for a field to be applied while measuring, making it difficult to quantify the anisotropy. SMOKE is ideal for anisotropy measurements because it allows *in situ* direct measurements of the local magnetization.

1.3 Antiferromagnetic ultrathin films

An antiferromagnet will spontaneously order below a critical temperature, called the Néel temperature (T_N), into a state where neighbouring spins are arranged antiparallel to each other resulting in zero net magnetization. This is referred to as the Néel transition, named after Louis Néel who was awarded the Noble prize for his discovery of antiferromagnetism [8]. Antiferromagnetic (AFM) ultrathin films are particularly difficult to study as they have the additional challenge of very small sample sizes that render standard bulk magnetic measurement techniques impossible. Even surface techniques used to make magnetic measurements cannot directly quantify the susceptibility of AFM ultrathin films. The limited experimental information on AFM systems [9], arising from their zero net magnetization, leaves potential for new phenomena to be found, possibilities for spintronic applications, and the discovery of the quantum ground state for AFM materials. An alternative approach is to measure the magnetic response indirectly by magnetically coupling an AFM ultrathin film with a ferromagnetic (FM) ultrathin film and then looking for changes in the FM susceptibility due to the presence of the AFM ultrathin film. A further discussion of measurement techniques and exchange coupling will be presented in the next chapter. Observing the Néel transition in an AFM ultrathin film is the second focus of this work.

Chapter 2

Theory

This chapter will examine the necessary theoretical background required to understand the experimental results. The first sections of this chapter will consider magnetic interactions in ultrathin film systems, with a particular focus on the magnetic anisotropy, followed by an introduction to the magnetic measurement techniques used in this work, and finally a discussion of coupled AFM and FM ultrathin films.

2.1 Magnetism

The magnetic field, **B**, can be broken down into two parts, the magnetization, **M**, and the **H** field. Mathematically this is expressed as [10]:

$$\mathbf{B} = 4\pi\mathbf{M} + \mathbf{H}. \tag{2.1}$$

$\mathbf{M}$ is dependent on the intrinsic properties of the particles in the system. In itinerant ferromagnets, the electron is by far the largest contributor to $\mathbf{M}$. Electrons have an intrinsic magnetic dipole moment, $\mathbf{m}$, because of their intrinsic charge and angular momentum. Intrinsic angular momentum, or spin, is a quantum mechanical phenomena. The $\mathbf{m}$ of an electron is given by equation 2.2:

$$\mathbf{m} = \mu_B \mathbf{S} \tag{2.2}$$

where μ_B is the Bohr magneton and $\mathbf{S}$ is the spin angular momentum. The azimuthal angular momentum is not included because the electrons are delocalized in metallic ferromagnets (such as Co). These electrons, called itinerant electrons, act as an electron gas. The angular momentum of an electron about a nucleus is quenched as the itinerant electrons are not confined to the region surrounding the nucleus. The magnetization is the sum of magnetic moments per volume of sample:

$$\mathbf{M} = \frac{1}{V} \sum^{N} \mathbf{m} \tag{2.3}$$

where N is the number of magnetic moments in volume V. The exchange and dipolar interactions, as well as the magnetic anisotropy, are the three phenomena that govern the magnetization.

The $\mathbf{H}$ field encompasses all components of the magnetic field $\mathbf{B}$ that are not due to the magnetization; its definition arises from equation 2.1:

$$\mathbf{H} \equiv \mathbf{B} - 4\pi\mathbf{M}. \tag{2.4}$$

The **H** field is created by electric currents and by fluctuations in the electric field.

2.2 Exchange interaction

The exchange interaction, a combination of Coulomb repulsion and the Pauli exclusion principle, is largely responsible for magnetic ordering in solids. The Pauli exclusion principle states that two indistinguishable fermions cannot exist in the same quantum state because the total wave function of a fermion system must be antisymmetric under fermion exchange. Electrons (which are fermions) that have different spin states can occupy the same space, resulting in an increase of the Coulomb energy. If electrons have the same spin state then they must be spatially separated, thus reducing the Coulomb energy. As this interaction concerns electrons cohabiting the same space, it is a short range interaction. The Heisenberg Hamiltonian is used to describe the exchange interaction, which is given by equation 2.5:

$$\mathcal{H}_{ex} = -J \sum_{i,j}^{NN} \mathbf{S}_i \cdot \mathbf{S}_j \tag{2.5}$$

where the sum is carried out over nearest neighbours and J is the exchange coupling constant. The sign of J dictates the magnetic ordering of a spin system. If J is positive then the energy is minimized when neighbouring spins are aligned parallel to each other such that the summation in equation 2.5 is maximized. The parallel alignment of spin is called ferromagnetism. FM materials (or ferromagnets) produce a large magnetization. When J is negative the spins are antiferromagnetically ordered, meaning neighbouring spins are arranged antiparallel to each other, minimizing the summation in equation 2.5. AFM materials (or antiferromagnets) have a zero net magnetization as there are equal contributions to the magnetization from opposite directions. Magnetic ordering occurs at temperatures where the exchange interaction is greater than the thermal energy. As mentioned above, the transition temperature for AFM systems is T_N; in FM systems the transition temperature is called the Curie temperature (T_C).

2.3 Dipolar interaction

The dipolar interaction in magnetic systems causes one magnetic dipole to align on the dipolar field produced by other dipoles. The energy of the dipolar interaction of N dipoles at the lattice sites r_i, due to the field of the N-1 other dipoles, is given by:

$$\mathcal{H}_{dip} = \frac{\Omega}{2} \sum_{i,j}^{N} \frac{1}{r_{ij}^3} \Big(\mathbf{S}_i \cdot \mathbf{S}_j - 3(\mathbf{S}_i \cdot \hat{\mathbf{r}}_{i,j})(\mathbf{S}_j \cdot \hat{\mathbf{r}}_{i,j}) \Big) \tag{2.6}$$

where Ω is a constant. The sum is carried over all dipoles in the system, $\mathbf{r}_{i,j}$ is the vector connecting the dipole at site i to that at site j, and $\hat{\mathbf{r}}_{i,j}$ is the unit vector associated with $\mathbf{r}_{i,j}$. The dipolar interaction shown in equation 2.6 is negligible at short range in comparison to the exchange interaction; however, it is the dominate long range magnetic interaction. In FM systems, the dipolar interactions between spins within a domain are additive, making the dipolar interaction one of the primary interactions between FM domains. Contrastingly, in AMF systems, antiparallel spins have opposing dipolar interactions, thus nullifying the long range effect.

The dipolar Hamiltonian promotes two different magnetic states in FM ultrathin films depending on whether the spins are aligned in or out of the film's plane. For spins that are aligned out of the plane of the film, the first term of equation 2.6 is minimized when spins are antiparallel to each other, as they would be in an antiferromagnet. The second term of equation 2.6 is zero because $r_{i,j}$ is perpendicular to $\mathbf{S_i}$ and $\mathbf{S_j}$ for the vast majority of lattice site pairs. The manifestation of the long range AFM dipolar interaction in FM films with out of plane spin alignment is the formation of striped FM domains of alternating up and down magnetization, producing a long range AFM effect [11].

In the scenario where the spins are aligned within the plane, the second term is minimized. The second term favours spins aligned head to tail along the vector between the spins. In this case a semi infinite number of spins can be aligned along the vector connecting the spins, making the second term of equation 2.6 dominant. The dipolar interaction will promote a single domain FM film.

The dipolar interaction is also responsible for demagnetization fields that arise in domains with their magnetization out of the plane; this is a short range effect of the first term of equation 2.6. Demagnetization fields are caused by uncompensated poles at surfaces or interfaces (analogous to the effect of surface charge in a polarized dielectric). The demagnetization field for an ellipsoid with constant magnetization is given by:

$$\mathbf{H}_{demag} = \overleftrightarrow{N}\mathbf{M} \tag{2.7}$$

where $\overleftrightarrow{N}$ is the second rank demagnetization tensor. $\overleftrightarrow{N}$ is dependent on the shape of the crystal, and the sum of its components must equal 1. N can be diagonalized along the principal axis of an ellipsoid [12]. For a sphere, $N_{xx} = N_{yy} = N_{zz} = 1/3$. A semi-infinite ultrathin film domain can be approximated to a flat ellipsoid, such that $N_{xx} = N_{yy} = 0$ and $N_{zz} = 1$; therefore, $\mathbf{H}_{demag} = N_{zz}M_z = M_z$. The demagnetization field (and the energy associated with it) is maximized when spins align perpendicular to the plane (maximum number of uncompensated poles at interfaces, $\mathbf{H} = M_z$), and is nullified for spins aligned in the plane (0 uncompensated poles at interfaces, $\mathbf{H} = 0$). The demagnetizing field thus promotes in-plane magnetization. This is the basis for shape anisotropy, which will be discussed more in the next section.

2.4 Magnetic anisotropy

Magnetic anisotropies are the directional dependancies of the magnetization on the physical structure of the crystal. Many of the unique phenomena occurring in ultrathin films can be attributed to magnetic anisotropies, as differences in atomic neighbourhoods and sample shape cause the anisotropies to vary greatly from that of the bulk [3]. The energy density associated with anisotropy is appropriately labelled the magnetic anisotropy energy density (MAE). As mentioned in section 1.2 there are three mechanisms for the magnetic anisotropy: shape anisotropy, magnetocrystalline anisotropy, and magnetoelastic anisotropy. The direction for which the MEA is minimized is called the easy axis, which is the preferred direction of magnetization. The hard axis is the least energetically favourable direction.

Néel [13] predicted that the anisotropy can be phenomenologically comprised of a surface contribution $[Energy/Area]$ that encompasses asymmetries at surfaces and interfaces, and volume contributions $[Energy/Volume]$ that are consistent throughout the film. The surface and volume contributions to the total anisotropies are made-up of the shape, magnetocrystalline, and magnetoelastic anisotropies. The total volume energy density of an ultrathin film, f_{tot}, multiplied by the thickness, t, gives the energy per unit area, σ_{tot}. It can be described by equation 2.8.

$$\sigma_{tot} = f_{tot}t = f_{bulk}t + f_{interface1} + f_{interface2} = f_{bulk}t + f_{surface} \qquad (2.8)$$

The subscripts “interface1” and “interface2” account for the film/substrate and the film/UHV interfaces having different contributions to the total anisotropy. The surface anisotropy is the sum of the two interface anisotropies. By examining how anisotropy varies with thickness, the surface and volume contributions can be isolated [3, 14] as the surface contribution will be independent of thickness and the volume contribution will be proportional to the thickness. This allows for the dominant contribution to the anisotropy (surface or volume) to be selected by changing the thickness of the film. Lattice dislocations that relieve interface induced strain lead to a nonlinear relation between the anisotropy and thickness.

2.4.1 Shape anisotropy

The shape anisotropy is caused by the demagnetization field, and is thus a consequence of the dipolar interaction (see section 2.3). The energy density due to shape anisotropy is given by:

$$f_{shape} = \frac{E_{shape}}{V} = 2\pi(\mathbf{M}\overleftrightarrow{N}\mathbf{M}). \tag{2.9}$$

For ultrathin films the demagnetization tensor N only has one non-zero element $N_z z$; therefore, equation 2.9 simplifies to:

$$f_{shape} = 2\pi\mathbf{M}^2\cos^2\theta \tag{2.10}$$

where θ is the angle between the magnetization and the surface normal. In-plane magnetization will be favoured as it reduces the energy density. Because it is a constant throughout the thickness of the film, the shape anisotropy is a volume anisotropy, but it manifests itself as a surface anisotropy due to its effect being independent of thickness.

2.4.2 Magnetocrystalline anisotropy

The inherent asymmetries of a lattice cause magnetocrystalline anisotropy. The spin-orbit interaction is primarily responsible for coupling the lattice anisotropies to the magnetization.

Itinerant ferromagnets like Co have delocalized electron band states whose occupancy is dependent on whether the state's energy is above or below the Fermi energy. In the Stoner model the exchange interaction will favour the spin up or down states lifting the degeneracy of spin band states. This causes the energy of states with favourable (unfavourable) spin orientation to drop below (rise above) the Fermi energy, which effectively populates (vacates) these states. The spin imbalance, resulting from the majority of occupied states having the favourable spin orientation, produces a net magnetization.

The band structure of a lattice is heavily dependent on the spatial charge distribution as Coulombic interactions are dominant within crystals. The orbital configuration dictates the spatial charge distribution, which in turn affects the spin band energies through the relativistic spin-orbit interaction, given by [15]:

$$\mathcal{H}_{SL} = -\lambda_o \mathbf{L} \cdot \mathbf{S} \tag{2.11}$$

where **S** is the electron spin and **L** is the orbital spin, which is related to the orbital configuration. The relativistic spin orbit coupling shifts the spin bands by causing hybridization of the spin states. In some **M** directions the shift in energy due to this interaction occurs in spin states near the Fermi energy, changing the overall system energy. The energy is dependent on the direction of the spin in relation to the charge distribution; this energy dependence is called an anisotropy energy.

For a hexagonal bulk crystal the volumetric contribution of the magnetocrystalline anisotropy energy density is phenomenologically given by the power series expansion:

$$f_C = K_2 \sin^2 \theta + K_4 \sin^4 \theta \tag{2.12}$$

where K_2 and K_4 are the anisotropy constants, and θ is the angle between the c axis and the magnetization. The energy is azimuthally isotropic according to equation 2.12 – a fair representation of experimental data [3]. For Co the magnetization prefers to lie uniaxially along the c axis (K_2 and K_4 are greater than zero). As the symmetry of the bulk environment is broken at the surface, the band structure and therefore the magnetocrystalline anisotropy must change at the surface, thus contributing to the surface anisotropy. It should be noted that without the magnetocrystalline anisotropy, ferromagnetism would not exist as the exchange and dipolar interactions are independent of the lattice construct.

2.4.3 Magnetoelastic anisotropy

Strain causes distortion of the crystal lattice; it is not surprising then that strain also contributes to the total magnetic anisotropy [16]. Anisotropy due to strain is called the magnetoelastic anisotropy, which is related to the phenomena of magnetostriction, where the crystal lattice is deformed in order to accommodate magnetic ordering in the sample [17]. The effects of magnetostriction are small ($\sim 1\%$ distortion) as the electrostatic energy holding the lattice together is much greater than that of the magnetic ordering. The magnetoelastic anisotropy is the inverse of magnetostriction, for it is concerned with how lattice deformations affect the magnetic ordering. A small lattice deformation will produce a small change in the electrostatic energy but can drastically affect the magnetic energy of the system [18]. Deformation of the lattice redistributes the charge, consequently altering the magnetocrystalline anisotropy as well; therefore, the magnetoelastic anisotropy is the change in the magnetocrystalline anisotropy due to strain. Consideration of the magnetoelastic anisotropy can be avoided by calculating the magnetocrystalline anisotropy from the band structure of the strained crystal. Despite this, calculating the magnetoelastic anisotropy is useful as it is more straight forward to compute and provides a comparison of the strained and unstrained anisotropies. The energy density due to the magnetoelastic anisotropy for an elastically isotropic medium is given by:

$$f(E) = \frac{3}{2}\lambda_m \sigma \cos^2 \psi \tag{2.13}$$

where σ is the stress, which is proportional to the strain *via* the elastic modulus γ ($\sigma = \varepsilon\gamma$). This leads to:

$$f(E) = \frac{3}{2}\lambda_m \varepsilon\gamma \cos^2 \psi \tag{2.14}$$

where λ_m is the constant that relates magnetostriction and strain, and ψ is the angle between the magnetization and the direction of strain. The factor of $\cos^2 \psi$ creates either an easy or a hard axis along the direction of strain, depending on the sign of λ_m and whether the strain is tensile or compressive. The energy density is linear with strain because the lattice spacing is far away from the magnetic equilibrium spacing.

The magnetoelastic anisotropy can differ greatly between films grown on different substrates [3], which must be regarded when making comparisons between experiments. In ultrathin films strain occurs during growth due to lattice mismatch between layers. The lattice mismatch is given by:

$$\eta = \frac{a_A - a_B}{a_A} \tag{2.15}$$

where a_A and a_B are the lattice constants of adjacent layers A and B. Two layers will stretch to fit each other below a critical thickness if η is not too large.

The layer with the larger lattice spacing will undergo compressive strain and the other layer will undergo tensile strain. The amount of strain experienced by each layer depends on the ratio of the elastic moduli: the film with the smaller modulus will experience more strain. The relative thickness of the films also contributes to the strain as a thicker film will have more bulk material that favours the bulk lattice spacing at the cost of limiting the flexibility of the interface layer. If the stretching occurs without introducing defects in the crystal, it is said to be in the "coherent" regime and the strain is described by equations 2.16 and 2.17:

$$\varepsilon_A = \frac{-\eta}{1 + \frac{\gamma_A t_A}{\gamma_B t_B}} \tag{2.16}$$

$$\varepsilon_B = \eta + \varepsilon_A \tag{2.17}$$

where γ_A and γ_B are the elastic moduli of layers A and B, with corresponding thicknesses t_A and t_b, respectively. Because the anisotropy energy density is dependent on film thickness, it becomes difficult to separate the magnetoelastic effects into volume and surface contributions unless $t_B \gg t_A$, when it can be attributed as purely a volume contribution. If the thickness is greater than the critical value, dislocations in the crystal appear in order to relieve the lattice of strain. This is called the incoherent regime. In this study the magnetoelastic anisotropy breaks the azimuthal symmetry of the magnetocrystalline anisotropy of a hexagonally packed film.

2.4.4 Representation as a field

The anisotropy can be represented as an effective field, $\mathbf{H}_{aniso}$, that acts upon the spins in the crystal. The relation between the anisotropy field and energy can be found by minimizing the free energy. The spins within a ferromagnet are subject to an effective field $\mathbf{H}_{eff}$ [19]:

$$\mathbf{H}_{eff} = -\frac{\partial f}{\partial \mathbf{M}} = -\frac{1}{M_s}\frac{\partial f}{\partial \phi} = \mathbf{H}_{aniso} + \mathbf{H}_{app} \tag{2.18}$$

where f is the total energy density, M_s is the saturation magnetization, ϕ is the angle between $\mathbf{M}$ and the easy axis, and $\mathbf{H}_{app}$ is the applied field. This assumes that $|\mathbf{M}| = M_s$. The energy density can be expressed by the following:

$$f = -K_{aniso}\cos^2\phi - \mathbf{M}\cdot\mathbf{H}_{app} = -K_{aniso}\cos^2\phi - M_s H_{app}\cos\theta \tag{2.19}$$

where K_{aniso} is the first order anisotropy constant and θ is the angle between the applied field and the magnetization. For the special case where the applied field is perpendicular to the easy axis, $\theta = \pi/2 - \phi$; therefore:

$$f = -K_{aniso}\cos^2\phi - M_s H_{app}\sin\phi. \tag{2.20}$$

At equilibrium the free energy is at a minimum and its derivative with respect to ϕ will be equal to 0:

$$\frac{\partial f}{\partial \phi} = 2K_{aniso}\cos\phi\sin\phi - M_s H_{app}\cos\phi = 0. \tag{2.21}$$

Rearranging, the equation provides an expression for H_{app}:

$$H_{app} = \frac{2K_{aniso}}{M_s} \sin\phi. \tag{2.22}$$

Representing the anisotropy contribution to the free energy as an anisotropy field, the free energy can be rewritten as:

$$f = -\mathbf{M} \cdot \mathbf{H}_{aniso} - \mathbf{M} \cdot \mathbf{H}_{app} = -M_s H_{aniso} \cos\phi - M_s H_{app} \sin\phi. \tag{2.23}$$

Differentiating with respects to ϕ at equilibrium gives:

$$\frac{\partial f}{\partial \phi} = M_s H_{aniso} \sin\phi - M_s H_{app} \cos\phi = 0, \tag{2.24}$$

which rearranges to become:

$$H_{app} = H_{aniso} \tan\phi \simeq H_{aniso} \sin\phi. \tag{2.25}$$

Combining equations 2.22 and 2.25 allows H_{aniso} to be expressed as:

$$H_{aniso} = \frac{2K_{aniso}}{M_s}. \tag{2.26}$$

The anisotropy field will lie along the easy axis. This is valid for small fields where ϕ is small. The field representation is a more convenient description because the anisotropy can easily be related to experimental quantities.

2.4.5 Anisotropy of ultrathin Co/W(110) films

The anisotropy of bulk *hcp* Co is given by equation 2.12, where $K_2 = 5.28 \times 10^6 \frac{\mathrm{erg}}{\mathrm{cm}^3}$ and $K_4 = 0.95 \times 10^6 \frac{\mathrm{erg}}{\mathrm{cm}^3}$ at room temperature [20, 21]. As mentioned in section 2.4.2, the magnetization prefers to lie along the c axis. The surface anisotropy also has a $\sin^2\theta$ dependence along the c axis and a surface anisotropy constant of $K_{surface} = 0.84 \frac{\mathrm{erg}}{\mathrm{cm}^2}$ [22].

For a Co film grown on W(110), the shape and magnetoelastic anisotropies must be considered. The magnetoelastic contribution can be estimated by looking at how the bulk lattices would stack on top of each other, as shown in figure 2.1. The Co lattice presents the *hcp* (0001) plane when grown on *bcc* W(110). The cubic lattice constant of bulk W is 3.16 Å, and the basal plane spacing for Co is 2.51 Å. The lattice mismatch defined in equation 2.15 gives a misfit of 20.5% along the W [001] direction and a misfit of -3.0% along the W $[1\bar{1}0]$ direction. The resulting Co structure has been reported to be dilated by 2.8% or 2.5% along the W$[1\bar{1}0]$ and compressed by 2.4% or 0.7% in the W[001] compared to the bulk structure by Pinkvos *et. al* [23], or the identical findings of Bansmann *et. al* [24] and Ociepa *et. al* [25]. Assuming a coherent structure, using equation 2.14, an elastic constant of $\sim 10^{12} \frac{\mathrm{dyne}}{\mathrm{cm}^2}$, and a magnetostriction constant of 5×10^{-5} [26], it is found that the in-plane magnetoelastic anisotropy is on the order of the magnetocrystalline anisotropy ($10^6 \frac{\mathrm{erg}}{\mathrm{cm}^3}$) present in the bulk. With the addition of shape anisotropy it is very reasonable for **M** to lie in the crystal plane. As the magnetocrystalline and shape anisotropies are relatively isotropic in the plane of the film, the symmetry of the strain selects the in-plane easy axis of magnetization along the W $[1\bar{1}0]$ axis. This strong uniaxial in-plane anisotropy was confirmed experimentally with spin-polarized low-energy electron microscopy (SPLEEM) by Pinkvos *et. al* [23]. They found that almost all domains contributed to micrographs with electrons polarized along the W$[1\bar{1}0]$ axis and only domains close to defects contributed to micrographs with electrons polarized along the W[001] axis. Later work by the same group [4] detected that a minority of spins were tilted out of the plane and that the tilt decreases with increasing film thickness ($\sim 35°$ at 3 ML and $\sim 5°$ at 8 ML). A qualitative measurement of the magnetocrystalline anisotropy was made by Kleibert *et. al* [27] using the transverse magneto-optic Kerr effect (T-MOKE).

Previous measurements using torsion oscillation magnetometry (TOM) of the anisotropy of epitaxial ultrathin Co/W(110) films by Fritzsche *et. al* provide an estimate for the surface and volume contribution of the in-plane anisotropy [1]. They have identified two different thickness regimes below and above a critical thickness, termed the coherent and incoherent regimes. In the coherent regime, the strain due to lattice mismatch (between the film and substrate) is the same throughout the volume of the film; therefore, the magnetoelastic anisotropy contributes to the volume anisotropy. The coherent regime includes films with thicknesses of 0 to < 2 nm (10 ML). In the incoherent regime, the strain due to lattice mismatch is relieved by stacking faults

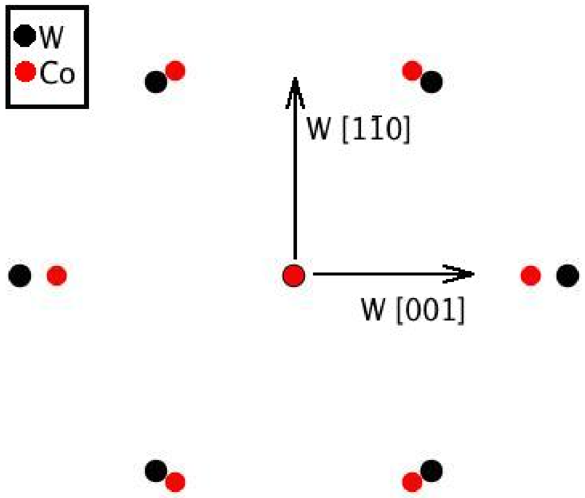

Figure 2.1: *Diagram of Co lattice (red) on top of W(110) plane (black). The cubic lattice constant of bulk W is* 3.16 $\mathring{A}$ *and the basal plane spacing for Co is* 2.51 $\mathring{A}$.

between layers, such that the magnetoelastic anisotropy contributes to the surface anisotropy as well. The incoherent regime includes films with thicknesses above $>$ 2 nm. The total volume contribution to the anisotropy for the coherent regime is estimated to be $2.5 \times 10^6 \frac{\mathrm{erg}}{\mathrm{cm}^3}$ and drops to $0.3 \times 10^6 \frac{\mathrm{erg}}{\mathrm{cm}^3}$ in the incoherent regime because of lattice relaxation. The surface contribution is negligible for the coherent regime and equal to $3 \times 10^7 \frac{\mathrm{erg}}{\mathrm{cm}^2}$ in the incoherent regime. Surprisingly, the critical thickness of 10 ML does not correspond to the onset of large magnetic domains at 6 ML, as found by Pinkvos *et. al* [23] for ultrathin Co/W(110) films. This could be due to differences in growth procedure.

2.5 Magnetic measurements

2.5.1 Magnetic susceptibility

The magnetic susceptibility is a measure of the ease of inducing magnetization, $\mathbf{M}$, in a sample in response to a magnetic field, $\mathbf{H}$. The susceptibility is defined by a second rank tensor in the limit of $\mathbf{H} \rightarrow 0$:

$$\chi_{i,j} = \frac{\partial \mathbf{M}_i}{\partial \mathbf{H}_j} \tag{2.27}$$

where $i, j =$ x, y, z. The easy axis of magnetization is usually chosen to be the x or z direction. The diagonal terms of χ will correspond to the change in magnetization along the easy and hard axes induced by fields along these axes. The susceptibility along the easy axis is called the longitudinal susceptibility because the change in magnetization is along the axis of magnetization (as shown in figure 2.2(a)). Longitudinal susceptibility corresponds to a change in the magnitude of the magnetization due to a spin reorientation, domain wall motion, spin reversal, or Curie transition. For a film with an easy axis in the plane of the film there will be two distinct transverse measurements (in and out of the plane). The ease of wiggling the magnetization away from the easy axis by applying a field in a direction perpendicular to it is called the transverse susceptibility (as shown in figure 2.2(b)). The extent of this wiggling is a measure of the magnetic anisotropy: the stronger the anisotropy the more difficult it is to tilt the magnetization away from the easy axis. The anisotropy energy is inversely proportional to the transverse susceptibility.

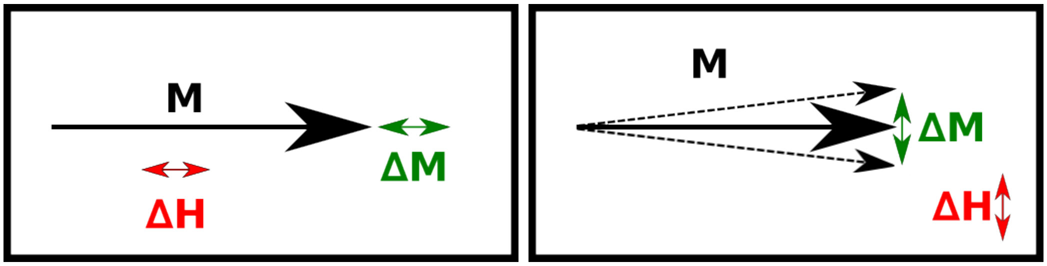

(a) (b)

Figure 2.2: *Diagram of a) longitudinal and b) transverse susceptibility. The magnetization,* **M***, is in black; the applied field,* **ΔH***, is in red; and the change in magnetization,* **ΔM***, is shown in green.*

In this work the in-plane transverse alternating current (ac) susceptibility will be measured by applying a small transverse alternating magnetic field in the plane and looking at the change in magnetization. By using a dual phase lock-in measurement technique, the ac susceptibility can be broken down into a real part (in phase with the applied field) and an imaginary part (out of phase by $\frac{\pi}{2}$):

$$\chi = \chi' + i\chi''. \tag{2.28}$$

The imaginary part corresponds to work done on the system by the magnetic field or, equivalently, dissipation of energy by magnetic degrees of freedom. Examples of phenomena that would contribute to the imaginary susceptibility include the reversal of spin blocks near a phase transition or the movement of domain walls over energy barriers due to structural defects.

2.5.2 Magnetic hysteresis loops

Magnetic hysteresis loops are a measurement of magnetization *versus* an applied direct current (dc) field. In paramagnetic and ferromagnetic systems the magnetization will reach a saturation value, $\mathbf{M}_s$, when a large enough field is applied, corresponding to all of the spins in the system aligning parallel to each other. The saturation field (the field required to saturate the magnetization) has a minimum along the easy axis. This work relies on hysteresis loops to quantify the saturation magnetization along the easy axis in order to calibrate measurements of the anisotropy energy density of ultrathin Co/W(110) films. The difference between the hard and easy axis saturation fields can be used for anisotropy measurements; however, these measurements will differ from small field results as the angle between the magnetization and the easy axis (ϕ in equation 2.18) will not be linear with $\mathbf{H}$ for large fields. Saturation fields along the hard axes are often too large to realize experimentally, as is the case in this work.

The hysteresis loop shown in figure 2.3 is of a FM 20 ML Co/W(110) film. The square shape of the loop suggests that there is domain wall motion across the area being probed. When the magnetic domain wall between spin up and down domains moves across the probing area, the measured magnetization will change as the spin up area becomes smaller and the spin down area becomes larger or *vice versa*. In order to move the domain wall the magnetic energy must overcome the pinning energy. Once unpinned, the domain wall is free to move, the magnetization changes sharply, and a square curve is produced. Pinning occurs at defects in the crystal lattice (grain boundaries, inclusions, vacancies, *etc.*) that cause a large local anisotropy. The flat top and bottom of the loop indicates that $\mathbf{M}_s$ is reached, although this could just be the saturation of one of several domains in the probing area. Another shape of hysteresis loop often occurs in FM systems because the probing area consists of many smaller domains. As the applied field overcomes the pinning energy for each domain, the magnetization increases slightly in the direction of the applied field; the addition of these slight increases produces a smooth continuous "S" shaped hysteresis loop.

2.5.3 Measuring the magnetic anisotropy

The magnetic anisotropy can be derived from the transverse susceptibility and the saturation magnetization. The effective field inside the sample is the vector sum of the anisotropy field and the applied field (as shown in figure 2.4). The angle ψ is also the angle between the tilted magnetization and the easy axis. Using the small angle approximation,

$$\tan\psi = \psi = \frac{4\pi\mathbf{H}_{ext}}{4\pi\mathbf{H}_{aniso}} = \frac{\mathbf{M}_{\perp}}{\mathbf{M}_s} \tag{2.29}$$

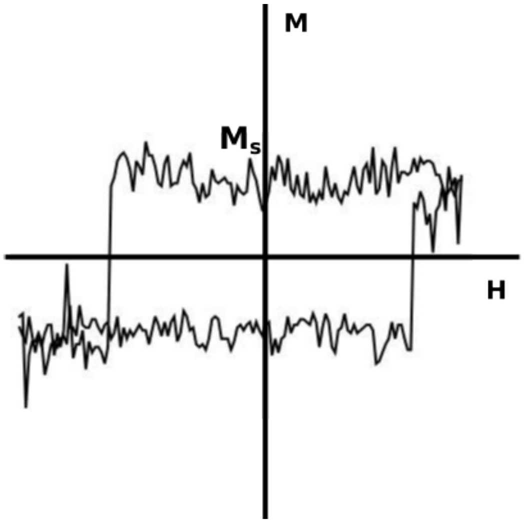

Figure 2.3: *Example of a hysteresis loop of a 20ML Co/W(110) film.* $\mathbf{M}_s$ *marks the saturation magnetization.*

where $\mathbf{M}_\perp$ is the component of the magnetization perpendicular to the easy axis, $\mathbf{H}_{aniso}$ is found by rearranging equation 2.29:

$$\mathbf{H}_{aniso} = \mathbf{M}_s \frac{\mathbf{H}_{ext}}{\mathbf{M}_\perp} = \frac{\mathbf{M}_s}{\chi_{trans}}. \tag{2.30}$$

By measuring χ_{trans} the need for very large fields to saturate the magnetization along the hard axis is avoided, enabling *in situ* measurements of the anisotropy.

2.6 AFM/FM coupled systems

Antiferromagnetism is difficult to observe using magnetometry as the macroscopic magnetization is zero. The additional challenge of the small sample size of an ultrathin film is that it is difficult to induce a sizeable moment by apply-

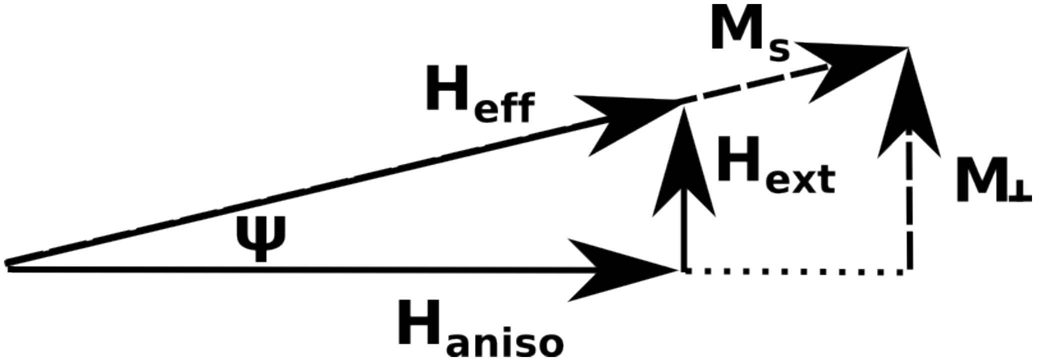

Figure 2.4: *Vector addition diagram for both magnetic fields and magnetization in the sample. The* **H** *and* **M** *triangles are similar; the magnetic deflection is exaggerated.*

ing a field. Conventional methods of probing magnetic structure in ultrathin films are not sensitive enough to directly observe antiferromagnetism. One approach to overcome these experimental limitations is to study AFM ultrathin films that are magnetically coupled to FM layers through their interface by the exchange interaction; this coupling is achieved by a bilayer film comprised of an AFM ultrathin film over a FM ultrathin film or *vice versa.* Instead of measuring the AFM signal directly, the magnetization of the FM ultrathin film is monitored and compared to that of an uncoupled FM ultrathin film. Deviations of magnetization in the coupled system from the uncoupled system are due to the magnetic ordering of the AFM layer acting on the FM layer through the interfacial exchange interaction.

2.6.1 Interfacial exchange interaction

The interfacial exchange interaction is an anisotropy between AFM and FM materials that was first discovered in 1956 by Meiklejohn and Bean [28] while studying oxidized Co. In order to observe the exchange bias it must be that $T_C > T_N$ [29], so that when field cooling, the FM layer is magnetically ordered before the AFM layer undergoes the Néel transition (as shown in figure 2.5(b)). The ordered FM spins at the interface impose a boundary condition on the AFM ultrathin film, which creates a preferential order to the film as it undergoes the Néel transition. Below T_N, the AFM/FM bilayer is locked into this preferred orientation (as shown in figure 2.5(c)). Applying a field does not affect the AFM layer because there is no net moment. The FM ultrathin film responds to the field, but is pinned by the AFM layer at their interface. Thus, the FM system experiences an additional surface magnetic anisotropy due to this interfacial exchange coupling. By characterizing the anisotropy of the FM layer it is possible to indirectly characterize the AFM layer; for example, its temperature dependence should reveal T_N.

Flipping the FM spins (as shown figure 2.5(d)) puts the system in a high energy spin configuration. In order to reduce its energy the system will create a domain wall or, for the case of thiner AFM ultrathin films, the spins in the AFM layer will flip as well. Unlike other anisotropies discussed thus far, interfacial exchange is unidirectional as opposed to uniaxial. In the case of demagnetized zero field cooled films there is still a local interfacial exchange;

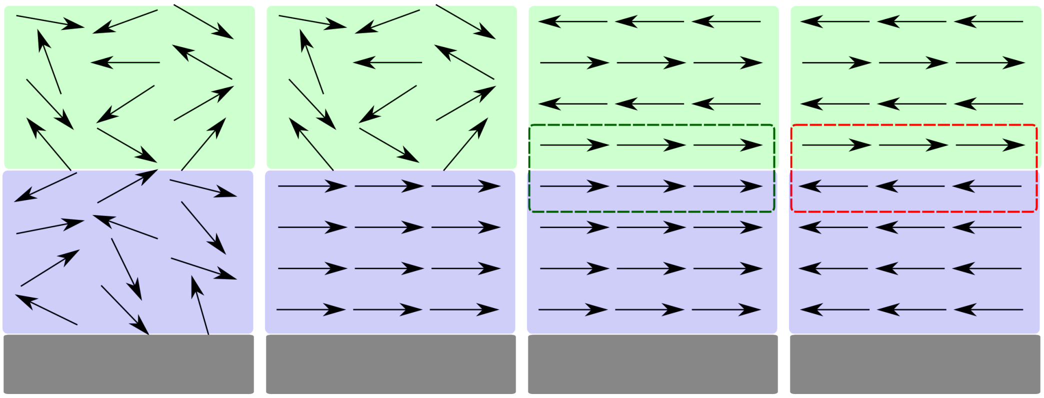

(a) $T > T_C > T_N$ (b) $T_C > T > T_N$ (c) $T_C > T_N > T$ (d) $T_C > T_N > T$

Figure 2.5: *Diagram of the interfacial exchange interaction. AFM and FM ultrathin films are shown in green and purple, respectively. a) Both FM and AFM ultrathin films are magnetically disordered. b) Below* T_C *the FM ultrathin film becomes ordered, thus setting a boundary condition on the ordering of the AFM ultrathin film. c) Below* T_N *the AFM ultrathin film orders according to the boundary set by the FM ultrathin film. d) Flipping the FM magnetization increases the energy of the system. Note that c) or d) could represent the preferred spin alignment at the boundary.*

however, there will not be a net bias because the domains will be randomly ordered. Interfacial exchange creates a unidirectional anisotropy so the energy density can be phenomenologically expressed by:

$$f_{ex} = K_{ex} \cos \psi \tag{2.31}$$

where K_{ex} is the anisotropy coefficient due to the interfacial exchange interaction. The hysteresis loop is characteristically affected by the interfacial exchange interaction [28]. The exchange bias causes a shift in the hysteresis loop of the FM layer along the applied field axis as a result of the interfacial exchange interaction being a unidirectional anisotropy.

K_{ex} is sample dependent as it is sensitive to the structural properties of the AFM ultrathin film [30]. The affect of the interfacial exchange increases with increasing interface roughness and decreases with increasing AFM crystallite size because these properties are related to the number of uncompensated spins present at the interface. Uncompensated spins are key to the interfacial interaction; therefore, a greater number of them enhances the affect of the interfacial exchange anisotropy. The energy required for AFM domain reversal affects the strength of interfacial exchange because, if the energy to flip a domain is small, an applied field will easily be able to flip both the FM and AFM domains.

2.6.2 Ultrathin CoO/Co/W(110) films

CoO is an AFM rock salt structure (as shown figure 2.6), where alternating (111) planes are composed entirely of Co or O. T_N for bulk CoO is 290 K. Above T_N, CoO is a paramagnetic material, while below T_N, in the AFM state, bulk CoO is a monoclinic structure due to magnetostriction (see section 2.4.3). This slight distortion from the cubic lattice is a combination of a tetragonal ($c/a = 0.988$ at 10 K) and a smaller trigonal distortion [31]. There has been much debate on the magnetic structure of AFM CoO since the 1950's [32, 33, 34, 35, 31, 36, 37]; yet, more experiments are needed to reach consensus [36, 37]. Jauch *et. al* [31] found that the spins from the Co^{2+} ions lie within the *ac* plane of the monoclinic structure, along the $[0.\bar{3}25, 0.\bar{3}25, 0.888]$ axis in reference to the cubic structure. The spins in each (111) plane are parallel to each other and are aligned antiparallel to the spins of neighbouring planes. The antiparallel alignment of consecutive planes produce a zero net magnetization. Additional anisotropies further complicate the determination of the axis of magnetization in ultrathin film systems.

To create exchange anisotropy, it is best to present the (111) plane of CoO at the interface, as this will ensure uncompensated spins at the interface. To promote the growth of the (111) plane, CoO films are grown on hexagonal substrates [38, 39]. Co/W(110) is a good candidate for the substrate as it has a hexagonal surface and $T_C > T_N$ for Co films thicker than 1.77 ML [40]. The rectangular centred lattice of the W(110) surface provides an

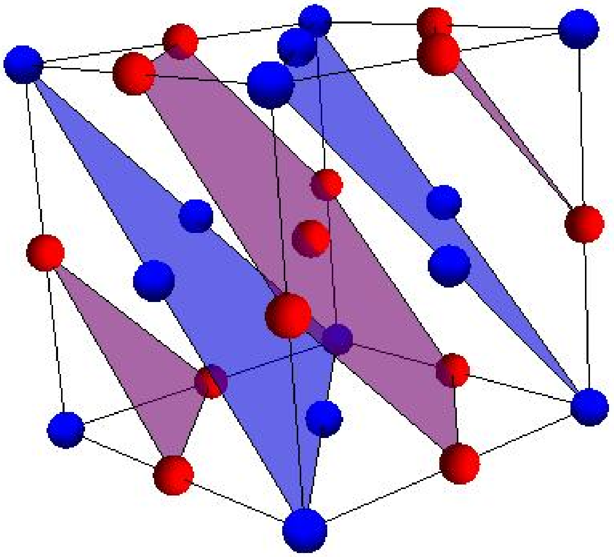

Figure 2.6: *3D representation of rock salt structure of CoO. Co atoms are in red and the O atoms are in blue.*

in-plane easy axis, removing the in-plane isotropy of bulk Co. The CoO/Co interface provides the strongest interfacial exchange interaction system in comparison with the other transition metals and their corresponding monoxides [41]. CoO/Co/W(110) is the ideal system to probe the Néel transition *via* the interfacial exchange interaction.

Chapter 3

Experimental Procedures

In this chapter the techniques used to produce, characterize, and probe the magnetic properties of ultrathin films will be discussed.

3.1 Ultrahigh vacuum systems

Ultrathin magnetic films are susceptible to surface contamination because of their large surface to volume ratio. To protect films from reactive gas contaminants, such as CO and O_2, films must be kept under ultrahigh vacuum (UHV) or capped by a nonmagnetic layer. By capping the magnetic film, *ex situ* measurements can be performed; however, the capping layer will interfere with the shape anisotropy and introduce strain in the system altering the magnetoelastic anisotropy of the magnetic film. *In situ* measurements allow the unaltered film to be examined. To do this, measurements must be conducted under UHV conditions, which are reached at pressures $\sim 10^{-10}$ Torr, so that films remain free of contaminants for 4 to 5 hours.

To achieve UHV conditions in the stainless steel vacuum chamber used in this work (see figure 3.1), a series of pumping techniques must be employed. First, a rotary pump is used to lower the pressure from atmospheric pressure (760 Torr) to 10^{-2} Torr. The rotary pump is left running continuously as a backing pump on the valve leading to the vacuum chamber in order to reduce the pressure gradient across the valves. At low enough pressures rotary pumps will leak oil vapours into the system, thus a molecular sieve trap is used to prevent contamination from oil vapours. The trap contains porous pellets that, due to their large surface area, are effective in absorbing oil vapours and other large molecules.

Once the system pressure reaches 2×10^{-1} Torr the cold trap is cooled by submersion in liquid nitrogen. The cold trap is a series of tubes placed inbetween the rotary pump and the system, such that it uses the rotary pump as a roughing pump. Gas molecules condense on the inner surfaces of the cold tubes, causing the pressure to decrease to $\sim 10^{-6}$ Torr.

The UHV valve is then closed, separating the cold trap and rotary pump from the system. The ion pump valve is opened to connect the ion pump (already at $\sim 10^{-9}$ Torr) to the system; this must be done slowly to avoid tripping the pump. The ion pump will run continuously and will bring the pressure down to $\sim 10^{-9}$ Torr. Because the ion pump works by absorption, it

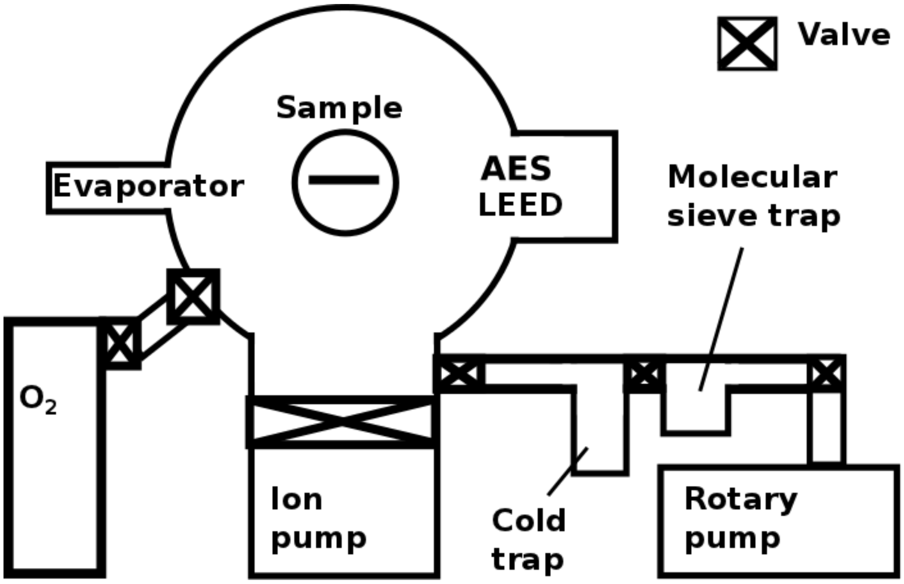

Figure 3.1: *Diagram of vacuum system. The ⊠ symbol represents a valve. The evaporator is used to grow the film. The AES and LEED apparatus is used to characterize the film.*

does not create any noise in optical measurements via mechanical vibrations and it can be contained within the vacuum chamber, which prevents leaks in the vacuum. The ion pump ionizes gas molecules with a plasma; the ions are then accelerated by an electric potential towards a titanium cathode. The collision between the ions and the cathode sputter titanium onto the surrounding surfaces. The elemental titanium will readily react with gas molecules (such as CO, CO_2, and O_2) to form solid compounds. Noble gases will not react with the titanium but may be trapped by sticking onto the cathode.

The system must be baked out to remove gases absorbed on the inner surfaces of the chamber by heating the system to 350-390 K in an oven for 12-48 h, depending on the amount of atmospheric exposure to which the surfaces were subjected. The pressure is monitored by an ion gage that will shut off the heating if the pressure rises past $\sim 10^{-6}$ Torr in order to protect the ion pump. Only with baking out can the ion pump reach 10^{-9} Torr. After baking out, the system is left to cool until it is safe to handle.

The final pumping system is the titanium sublimation pump (TSP), which brings the pressure from 10^{-9} Torr to the UHV regime ($\sim 10^{-10}$ Torr). The TSP is composed of a thick titanium filament that is heated by a high ac current (45 A). When first turned on, the pressure increases due to gases leaving the surface of the filament; further heating causes titanium to sublimate on to the surrounding surfaces. Gas molecules will react with titanium surfaces to form solid compounds reducing the pressure, as they did in the ion pump.

The filaments of components used to grow films and take measurements must be heated up to remove any residual gases by running a current through each filament for 45 min in a process called degassing. After each filaments is heated the TSP is used to trap the escaped gases.

3.2 Sample holder and substrate

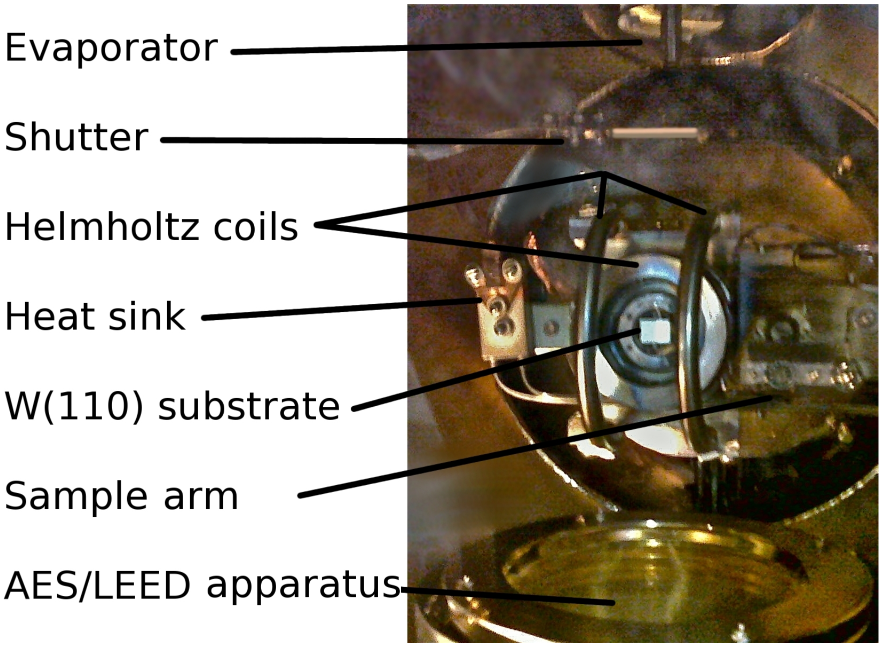

Figure 3.2: *Photograph of sample holder from the top window of the vacuum chamber. The thermocouple and heating coil are obscured from view by the Helmholtz coils and substrate, respectively.*

The sample holder (figure 3.2) used in this work has three degrees of translational motion and two degrees of rotational motion, which are necessary to align the sample for film growth and different measurement techniques. As shown in figures 3.1 and 3.2, the evaporator and Auger electron spectroscopy (AES)/low energy electron diffraction (LEED) apparatus are on opposite sides of the vacuum chamber. The sample holder has an axis of rotation out of the page of figure 3.1 and along the sample arm in figure 3.2, while holding the substrate in the centre of the chamber, so that it can rotate to face either system. The other axis of rotation is normal to the plane (vertical line along the centre of figure 3.1 and out of the page in figure 3.2), enabling the sample to rotate relative to a pair of Helmholtz coils used to provide an applied in-plane magnetic field. This permits magnetic measurements along different crystallographic directions. There is a second pair of Helmholtz coils that are normal to the plane, which provide an out of plane field.

A $W_{95}Rh_5/W_{74}Rh_{26}$ thermocouple is embedded in a hole in the side of the substrate. A W filament behind the substrate can heat the substrate *via* radiation or electron bombardment. Radiative heating can be used to raise the temperature of films up to $\sim$ 600 K, while electron bombardment cleans the substrate and reaches $\sim$ 2500 K. To achieve electron bombardment, a large potential difference of $\sim$ 2 kV is applied between the filament and the substrate, then a current of $\sim$ 3 A is run through the filament. High energy electrons will overcome the work function of the filament and be accelerated towards the substrate, thus colliding with it and heating it up. The substrate is also thermally connected to a heat sink that can be used to cool the substrate to a minimum of 115 K. The heat sink is cooled by a pipe that carries liquid nitrogen in and out from outside the vacuum chamber.

This work uses a single crystal of W with dimensions of $1.1 \times 0.6 \times 0.2$ cm^3, cut to show the W (110) plane (as shown in figure 3.2). W is used for the substrate for numerous reasons. It has a high melting temperature so its surface can be cleaned by heating it to temperatures at which other molecules will desorb from its surface. W does not contribute a magnetic moment to the system as it is paramagnetic. High surface energy prevents diffusion of other atoms into the W substrate and promotes surface wetting [23]. W is not reactive with other elements in the system. C is an exception and readily forms WC, a very stable compound even at high temperatures.

C contaminants are introduced to the system whenever it is opened for maintenance. To remove these contaminants, the substrate is heated to ~ 1000 K by electron bombardment in an O_2 atmosphere of 3×10^{-6} Torr. O_2 strips WC of its C to form CO and CO_2. The presence of carbon on a W(110) substrate changes the structures of Co films from the *hcp* (0001) surface to the *fcc* (100) surface [23, 42], which affects the band structure and consequently the magnetic anisotropy of the Co film. To ensure all experimental results are free from C contamination, the amount of C on the film is determined by AES.

3.3 Auger electron spectroscopy

AES is a surface analysis technique that uses the unique electron energy configurations of atoms to identify the composition of a surface [43]. This method measures the number of Auger electrons emitted from a surface as a function of the emission energy.

A beam of monoenergetic electrons, accelerated by an electron gun, is incident normally on a surface [44]. The emitted Auger electrons are analyzed by a series of concentric semi-spherical gold grids. The grids are centred around the point of contact between the electron beam and the surface. The electric potential of the grids are set such that they can only be traversed by electrons with energies greater than a certain energy. The transmitted electrons are picked up by a semi-spherical screen that is concentric with the grids. The number of transmitted electrons at a certain energy is directly measured using the current flowing from the screen to ground. A diagram for the AES setup is shown in figure 3.3; the charge coupled device (CCD) camera is part of the LEED apparatus, which shares the electron gun and screens.

AES is only concerned with Auger electrons that arise when a core electron is removed by a collision with an electron from the incident beam, leaving a low energy vacancy in the atom (depicted in figure 3.4(a)). An electron from a higher energy level will drop down to fill the vacancy, either producing an X-ray or transferring energy to another electron of a similar initial energy. If energy is transferred between electrons, the electron that gains energy is

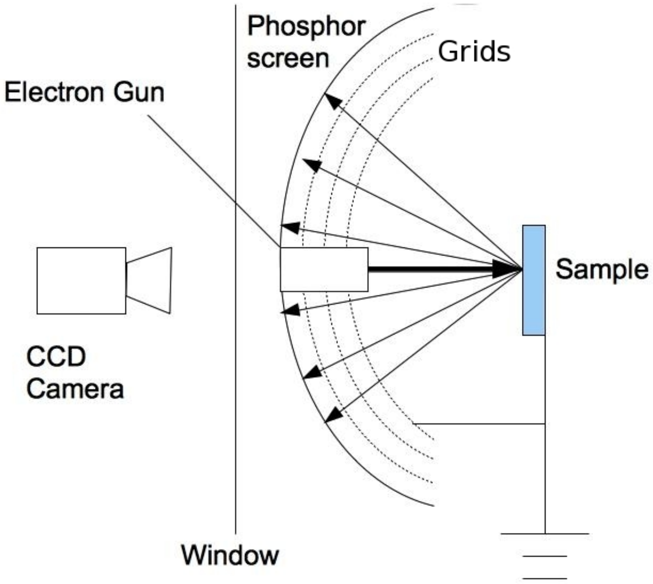

Figure 3.3: *Diagram of AES and LEED apparatus. The electron gun provides a beam of monoenergetic electrons that are diffracted off the sample at a normal angle. Gold screens are set at electric potentials such that only electrons with energies greater than a particular energy can pass through and be detected by the phosphorous screen.*

emitted with a kinetic energy equal to that of the transition energy of the other electron (as shown in figure 3.4(b)). The emitted electron is called an Auger electron, and has an energy characteristic of its parent atom. Auger electrons provide information from only the surface atoms as they have a short elastic mean free path (~ 10 Å).

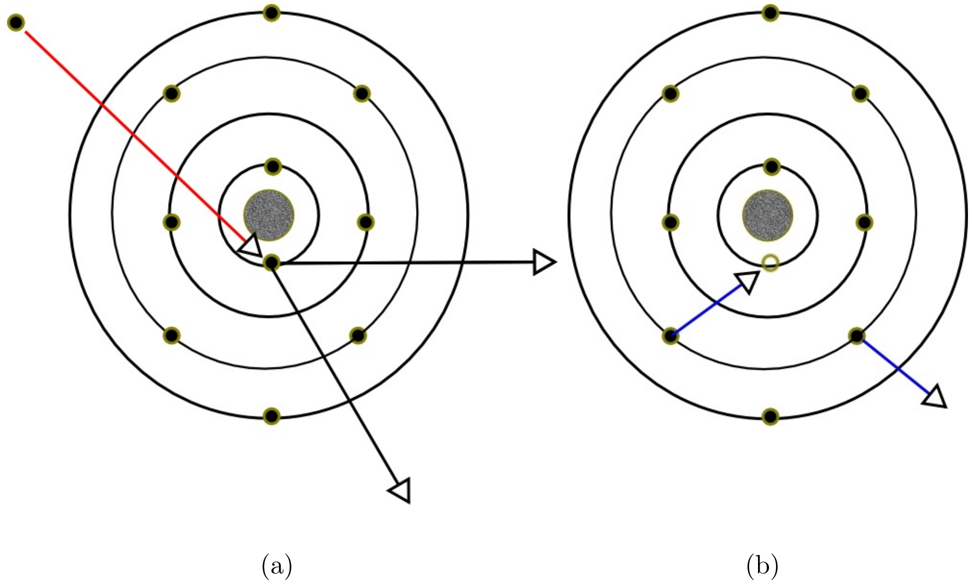
(a) (b)

Figure 3.4: *Diagram of creation of an Auger electron. a) Low energy core electron is removed via collision with an electron from an electron beam. b) Higher energy electron transitions to fill vacancy and Auger electron is emitted to conserve energy.*

The majority of detected electrons come from secondary back scattered electrons instead of Auger electrons. The energy spectrum of secondary back scattered electrons is smooth but large in comparison to that of Auger electrons. In order to isolate the information from the Auger electron spectrum, the derivative of the total electron distribution is taken; peaks in the Auger spectrum are sharp so they create large peaks in the derivative of the distribution. The Auger spectrum of the W(110) substrate from 150-190 eV is shown in figure 3.5.

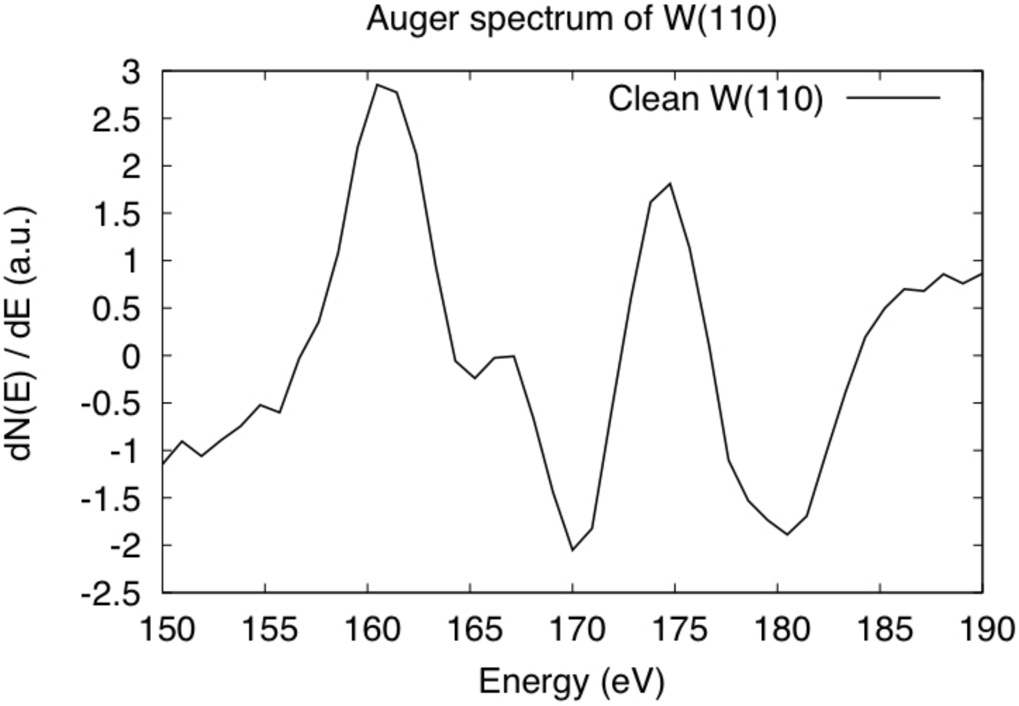

Figure 3.5: *Auger spectrum of W(110) substrate. This spectrum is used as a reference spectrum for film thickness calibration.*

AES is used in this work to determine film thickness and to identify the growth mode by monitoring the amplitude of the spectrum from the substrate and that of the film material as a function of the growth time. As a film grows the spectrum of the substrate is attenuated. The attenuation is defined as the fraction by which the clean substrate Auger spectrum is multiplied to produce the substrate spectrum when a film is present. Figure 3.5 is the reference spectrum for thickness calibration for films grown on W(110). Counterintuitively, the attenuation is said to increase when this fraction decreases. A graph of attenuation *versus* growth time is called an uptake curve (as shown in figure 3.6).

There are three different growth modes for epitaxial ultrathin films. In the Frank-van der Merwe (FvdM) growth mode, full layers of atoms are completed layer by layer (see figure 3.7(a)). For this to occur the surface energy of the substrate must be greater than the addition of the surface energy of the film material and the interface energy. The amplitude of the Auger spectrum of the substrate is reduced (attenuation increases) linearly with coverage until the first monolayer is complete because the amount of covered substrate is proportional to the completeness of the layer. The second monolayer increases the coverage but, because the attenuation depends exponentially on thickness, the second layer cannot change the attenuation at the same rate as the first. The attenuation increases linearly as the second layer completes with a smaller slope, as seen in figure 3.6. Subsequent layers have smaller and smaller linear rates of increasing coverage. The rates decrease exponentially as a function of the number of completed layers. By plotting the uptake curve, the time taken to complete one monolayer can be identified by the first kink in the curve (where the rate changes) and used as a calibration for thickness of the film for

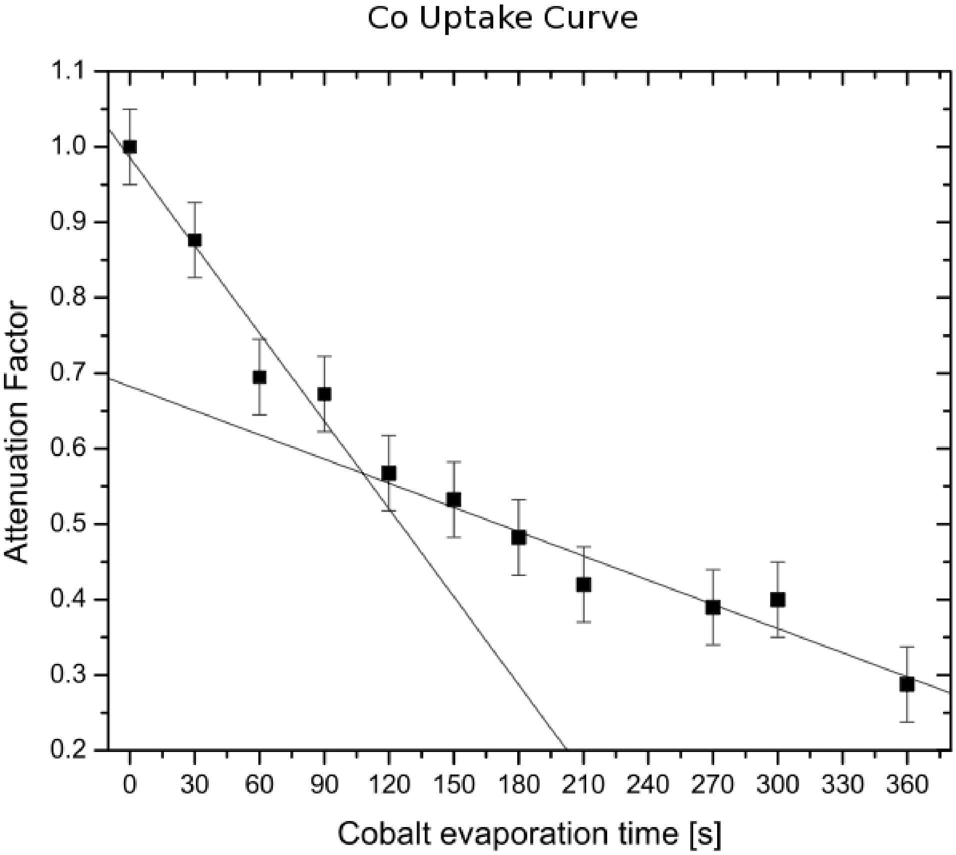

Figure 3.6: *Uptake curve of Co on a W(110) substrate. A Stranski-Krastanov (SK) growth mode is observed, with the completion of the first monolayer occurring after a growth time of 105 s.*

varying growth times.

The other two growth modes have substrate surface energies less than the sum of the surface energy of the film material and the interface energy. The Volmer-Weber (VW) growth mode minimizes coverage of the substrate by forming islands of the film material that will be several monolayers thick before the first monolayer is complete (see figure 3.7(c)). The uptake curve is exponential with no features indicating the completion of a monolayer. In the Stranski-Krastanov (SK) growth mode the first monolayer is completed before islands form for higher film thicknesses (as shown in figure 3.7(b)). There is a kink in the uptake curve corresponding to the completion of the first monolayer, so the growth time per monolayer can be found. The first monolayer will complete because the film atoms wet the substrate.

The uptake curve for Co grown on the W(110) substrate is shown in figure 3.6. The kink indicating the completion of the first monolayer occurs at a growth time of 105 s. This growth time is used as a calibration for the evaporator so that films of a known thickness can be grown (see section 3.5). The film grows in the SK growth mode as there is not an obvious kink at 210 s, where two monolayers would have formed in the FvdM growth mode.

3.4 Low energy electron diffraction

LEED is an elastic scattering technique for examining the 2D structure of surfaces [45]. The diffraction patterns obtained from LEED can also be used to

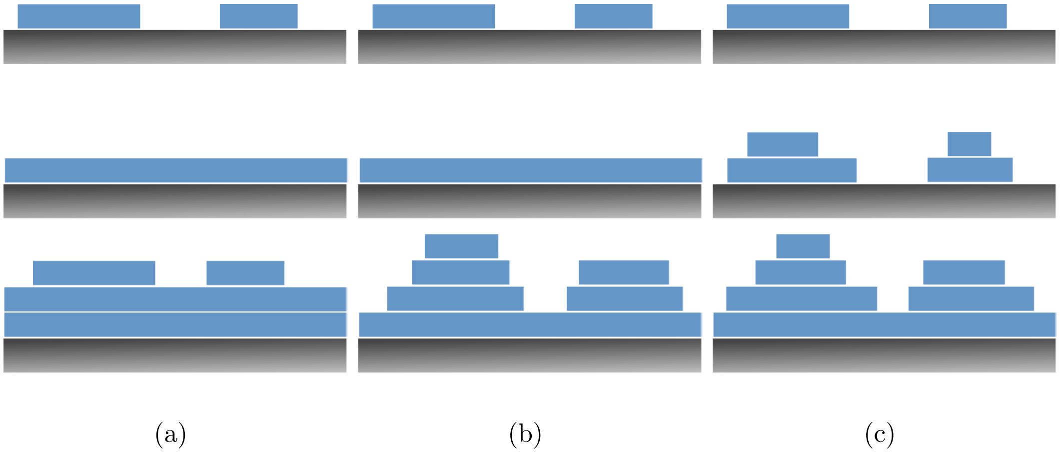
(a) (b) (c)

Figure 3.7: *Diagram of growth modes of ultrathin films for different amounts of growth material: top < 1 ML, middle 1 ML, bottom > 2 ML. The substrate is shown in grey and growth material is shown in blue 1 ML thick rectangles. a) Frank-van der Merwe (FvdM) growth mode; monolayers are completed one after another. b) Stranski-Krastanov (SK) growth mode; the first monolayer is completed then island growth starts where some regions of the film are thicker than others. c) Volmer-Weber (VW) growth mode; island growth begins before the first monolayer is complete. The first monolayer is completed when islands merge together.*

determine the uniformity of a film and the strain in the crystal, thus providing a prediction for the magnetoelastic anisotropy [1]. By observing the intensity of the LEED peaks as a function of beam energy, the inter-planar spacing can be inferred from Bragg's law.

Figure 3.3 shows the AES and LEED apparatus. A monoenergetic beam of electrons emerging from the electron gun strikes the sample perpendicular to its surface. The backscattered electrons are collected by a series of grids (described in section 3.3) set at electric potentials such that only elastically diffracted electrons can pass through them. Once through the grids, the elastically scattered electrons are accelerated onto a phosphorous screen with a 5 kV potential. The absorption of an electron by the phosphorous screen releases a photon, allowing for the electron diffraction pattern to be viewed through a window by eye or a CCD camera. To reduce noise, 50 images are averaged to form one image for each LEED pattern.

The energy range of LEED (20-300 eV) ensures that only the surface of the sample is probed; therefore, the diffraction pattern will be characteristic of the 2D surface structure. An elastically scattered electron with an initial linear momentum perpendicular to the substrate will be reflected in the opposite direction from which it came unless it gains crystal momentum from the lattice along the plane of the film. When this occurs the momentum parallel to the surface possessed by the reflected electron ($\mathbf{k}'_{\parallel}$) is given by equation 3.1:

$$\mathbf{k}'_{\parallel} = \mathbf{k}_{\parallel} + \mathbf{G} \tag{3.1}$$

where $\mathbf{k}_{\parallel}$ is the initial parallel wave vector $(= 0)$ and $\mathbf{G}$ is a reciprocal lattice vector of the film surface. The displacement of electrons parallel to the surface creates a picture of the surface's reciprocal lattice, which is observable because of the fluorescence produced by electrons hitting the phosphorous screen. The diffraction pattern describes the symmetries present on the surface of the lattice, and can be used to quantitatively find the reciprocal lattice vectors by the geometry of the LEED setup or through comparing to the diffraction pattern of a known surface. In this work all LEED measurements are made comparatively to the W(110) LEED pattern, as the pattern is well defined and the reciprocal and real lattice structure is known. The geometrical approach is not favoured because variations in the spherical grids distort the pattern. The real space primitive lattice vectors ($\mathbf{a}_1$ and $\mathbf{a}_2$) of the surface can be obtained from the primitive reciprocal lattice vectors ($\mathbf{b}_1$ and $\mathbf{b}_2$) using the following relations,

$$\mathbf{a}_1 = 2\pi \frac{\mathbf{b}_2 \times \hat{\mathbf{n}}}{\mathbf{b}_1 \cdot (\mathbf{b}_2 \times \hat{\mathbf{n}})} \tag{3.2}$$

$$\mathbf{a}_2 = 2\pi \frac{\hat{\mathbf{n}} \times \mathbf{b}_1}{\mathbf{b}_2 \cdot (\hat{\mathbf{n}} \times \mathbf{b}_1)} \tag{3.3}$$

where $\hat{n}$ is the unit vector normal to the surface. $\mathbf{G}$ in equation 3.1 is a linear combination of primitive reciprocal lattice vectors $\mathbf{b}_1$ and $\mathbf{b}_2$.

Figure 3.8 shows a negative LEED image for the W(110) surface, with incident electrons having an energy of 139.0 eV. The electron gun appears as the shadow of a centred circle with an extending support arm that blocks the central diffraction spot. The faint shadow of a set of Helmholtz coils is seen as two horizontal bars above and below the diffraction spots in figure 3.8. The primitive reciprocal lattice vectors are labelled $\mathbf{b}_1$ and $\mathbf{b}_2$, and are given as follows:

$$\mathbf{b}_1 = \frac{2\pi}{a_W}(\hat{x} + \frac{\hat{y}}{\sqrt{2}}) \qquad \mathbf{b}_2 = \frac{2\pi}{a_W}(\hat{x} - \frac{\hat{y}}{\sqrt{2}}). \tag{3.4}$$

Using equations 3.2 and 3.3 the real space lattice vectors are found to be:

$$\mathbf{a}_1 = a_W(\frac{\hat{x}}{2} + \frac{\hat{y}}{\sqrt{2}}) \qquad \mathbf{a}_2 = a_W(\frac{\hat{x}}{2} - \frac{\hat{y}}{\sqrt{2}}) \tag{3.5}$$

where $\mathbf{a}_1$ and $\mathbf{a}_2$ correspond to a rectangular centred lattice that is expected for the (110) plane of *bcc* crystals such as W. The constant a_W is the cubic lattice constant of W, which is equal to 3.16 Å. The magnitude of these vectors is needed to calculate the lattice constant of other surfaces:

$$|\mathbf{b}_1| = |\mathbf{b}_2| = b_W = \sqrt{\frac{3}{2}}\frac{2\pi}{a_W} \tag{3.6}$$

and

$$|\mathbf{a}_1| = |\mathbf{a}_2| = \frac{\sqrt{3}}{2}a_W. \tag{3.7}$$

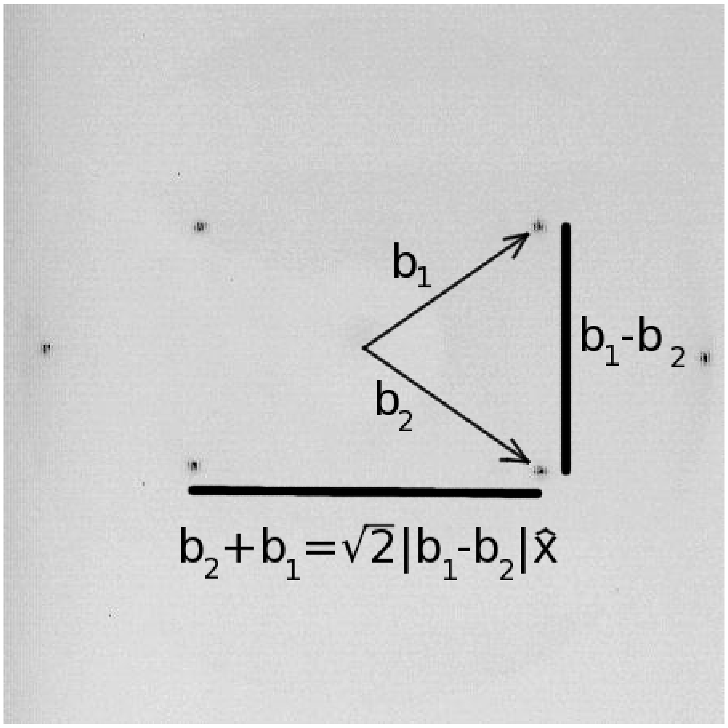

Figure 3.8: *Negative LEED image of W(110) substrate. The energy of the incident electron beam is 139.0 eV. The primitive reciprocal lattice vectors* $\mathbf{b}_1$ *and* $\mathbf{b}_2$ *are shown as well as their sum and difference. The shadow of the electron gun and Helmholtz coils are faintly visible.*

As mentioned above, the W(110) surface is used to convert reciprocal lattice vectors to real space measurements. In order to obtain information on a hexagonal lattice from comparing its LEED pattern to that of the centred rectangular surface of W(110), a conversion factor is needed, especially if the two diffraction patterns are of different incident energies. The lattice vectors and corresponding reciprocal lattice vectors of a hexagonal structure are given below:

$$\mathbf{a}_{1hex} = a_{hex}(\frac{\hat{x}}{2} + \frac{\sqrt{3}\hat{y}}{2}) \qquad \mathbf{a}_{2hex} = a_{hex}(\frac{\hat{x}}{2} - \frac{\sqrt{3}\hat{y}}{2}) \tag{3.8}$$

and

$$\mathbf{b}_{1hex} = \frac{2\pi}{a_{hex}}(-\hat{x} - \frac{\hat{y}}{\sqrt{3}}) \qquad \mathbf{b}_{2hex} = \frac{2\pi}{a_{hex}}(-\hat{x} + \frac{\hat{y}}{\sqrt{3}}). \tag{3.9}$$

The constant a_{hex} is the basal plane lattice constant of a *hcp* structure. Note that

$$|\mathbf{a}_{1hex}| = |\mathbf{a}_{2hex}| = a_{hex} \tag{3.10}$$

and that

$$|\mathbf{b}_{1hex}| = |\mathbf{b}_{2hex}| = b_{hex} = \frac{2}{\sqrt{3}}\frac{2\pi}{a_{hex}}. \tag{3.11}$$

Using the quotient of equations 3.6 and 3.11, the following expression provides a solution for a_{hex} in terms of b_W, b_{hex}, and a_W:

$$\frac{a_{hex}}{a_W} = \frac{2\sqrt{2}}{3}\,\frac{b_W}{b_{hex}}. \tag{3.12}$$

Unfortunately the reciprocal lattice vectors b_W and b_{hex} are not measured directly and must be calculated. From the energy equation of a free electron, an expression of $\mathbf{k}'_{\|}$ (see equation 3.1) is given by:

$$\mathbf{k}'_{\|} = \sqrt{\frac{2m_eE}{\hbar^2}}\sin\theta = \sqrt{\frac{2m_eE}{\hbar^2}}\frac{x}{R} \tag{3.13}$$

where E is the energy of the incident beam, $\hbar$ is the reduced Planck's constant, m_e is the mass of an electron, θ is the angle between the electron trajectory and the surface normal, x is the displacement parallel to the surface, and R is the radius of the screen. $\mathbf{k}'_{\|}$ is equivalent to $\mathbf{G}$, which is a linear combination of reciprocal lattice vectors $\mathbf{b}$. For primary diffraction points, $\mathbf{k}'_{\|} = \mathbf{b}$, which provides the following equality:

$$\frac{b_W}{b_{hex}} = \sqrt{\frac{E_W}{E_{hex}}}\frac{x_W}{x_{hex}} \tag{3.14}$$

where E_W and E_{hex} are the energies of the incident electron beam and x_W and x_{hex} are the distances from the centre of the LEED pattern to the diffraction peak for the W and hexagonal LEED images, respectively. Equation 3.12 thus becomes:

$$\frac{a_{hex}}{a_W} = \frac{2\sqrt{2}}{3}\sqrt{\frac{E_W}{E_{hex}}}\,\frac{x_W}{x_{hex}}. \tag{3.15}$$

The quantities in equation 3.15 are measurable from the electron beam control and the LEED pattern.

The variation of the intensity of the central diffraction spot with changing energy can be used to determine the inter-planar spacing. For an initial electron beam normal to the surface, resonance beam energies corresponding to maxima in the intensity of the central LEED spot will satisfy the Bragg condition:

$$d = \frac{n}{2}\lambda \tag{3.16}$$

where d is the inter-planar spacing, n is the diffraction order, and λ is the de Broglie wavelength. The relationship between the resonance energies and the corresponding diffraction order is shown in equation 3.17,

$$\frac{E}{n^2} = \frac{h^2}{8m_e d^2} \tag{3.17}$$

where h is Planck's constant. Equation 3.17 is only valid for an incident beam normal to the surface; otherwise, a factor of $\cos\theta$ (θ being measured from the plane normal) must be included. Experimentally the incident beam is tilted by $\sim 7^\circ$ from the normal so that the central diffraction spot is not obscured by the shadow of the electron gun. This angle is small enough to be approximated as a normal incidence. The energy can be plotted *versus* the diffraction order squared and the slope can be used to solve for the inter-planar lattice spacing. Figure 3.9 shows the energies corresponding to LEED intensity maxima of the central diffraction spot for the W(110) surface. The spacing is found to be 2.23 ± 0.01 Å using equation 3.17, which agrees with the expected value of 2.23 Å. Because the crystal is almost perfectly ordered, intensity peaks can be observed at much higher frequencies; however, this is not the case for thin films where peak intensity maxima become very difficult to identify above $\sim 300\ eV$. Only the very bright maxima were used in this graph as dimmer local maxima occur due to multiple scattering events. Multiple scattering is only a concern for well ordered crystals as it will not contribute extra intensity peaks in ultrathin films. Determining what is the diffraction order corresponding to the first observed resonance energy is not trivial and requires fitting E *versus* n^2 to a straight line.

3.5 Ultrathin film growth

3.5.1 Ultrathin metallic films

Magnetic ultrathin films are often made of Co, Ni, and Fe, which are all FM metals. These metallic ultrathin films can be grown effectively using evaporation in UHV.

The evaporator in figure 3.10 uses electron bombardment to heat up the metal source wire (purity > 99.99%). A high current (3.5 A) is passed through the filament, fil, near the metal source that acts as a supply of thermally emitted electrons. A high voltage (1.75 kV) is applied to the source, which

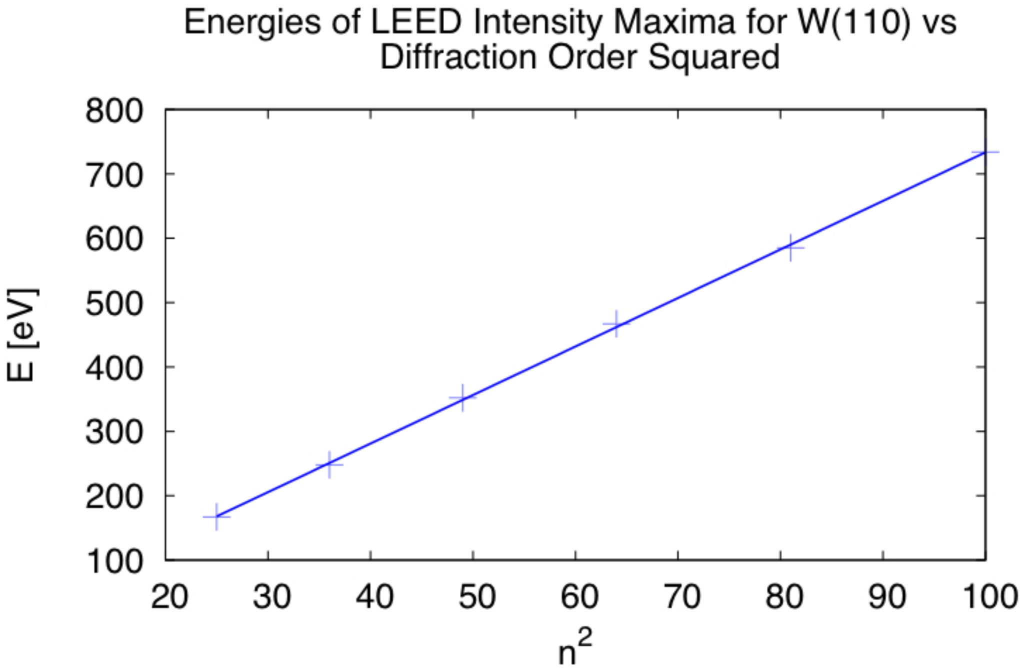

Figure 3.9: *Plot of the energies of LEED intensity maxima of the central diffraction spot* versus *diffraction order for W(110). The slope corresponds to a spacing of* 2.23 ± 0.01 $\mathring{A}$. *The energy range is much larger than normally used for LEED, which is acceptable because the crystal is uniform with depth. For ultrathin films intensity peaks are rarely observed above* $\sim 300\ eV$.

is then is advanced towards the filament by the retractable holder that can be controlled from outside the vacuum. As the source is nearing the filament, the thermally emitted electrons are accelerated and focussed onto the tip of the wire. The heat from the electrons striking the source melt the tip of the metal and causes metal atoms to evaporate into the vacuum. The evaporated atoms are collimated into a beam by a pair of apertures, ap1 and ap2, and strikes the sample normal to its surface. The second aperture is isolated from ground and kept at a potential of +23 V to attract evaporated atoms that were ionized by the bombarding electrons. The ion current from this wire, IC, is a measure of the atomic flux exiting the evaporator onto the sample. The ion current is held constant during evaporation by adjusting the position of the source metal relative to the filament to ensure a constant rate of growth. The bombardment current measured by the high voltage wire is also monitored during evaporation as it indicates the amount of metal being evaporated. The bombardment current is not affected by additional ionized gas, which occurs when growing a film in the presence of O. The evaporator is water cooled to prevent gases from desorbing from its components.

The room temperature thickness calibration from the uptake curve in figure 3.6 equates a thickness of 1 ML Co with 105 s of Co evaporation at an ion current of 1.0 nA (1 ML = 1.75 nA min), corresponding to a growth rate of 0.57 ML/min. Ultrathin films grown at room temperature showed the sharpest LEED diffraction spots. Above $\sim$ 400 K (420 K in bulk) Co undergoes a

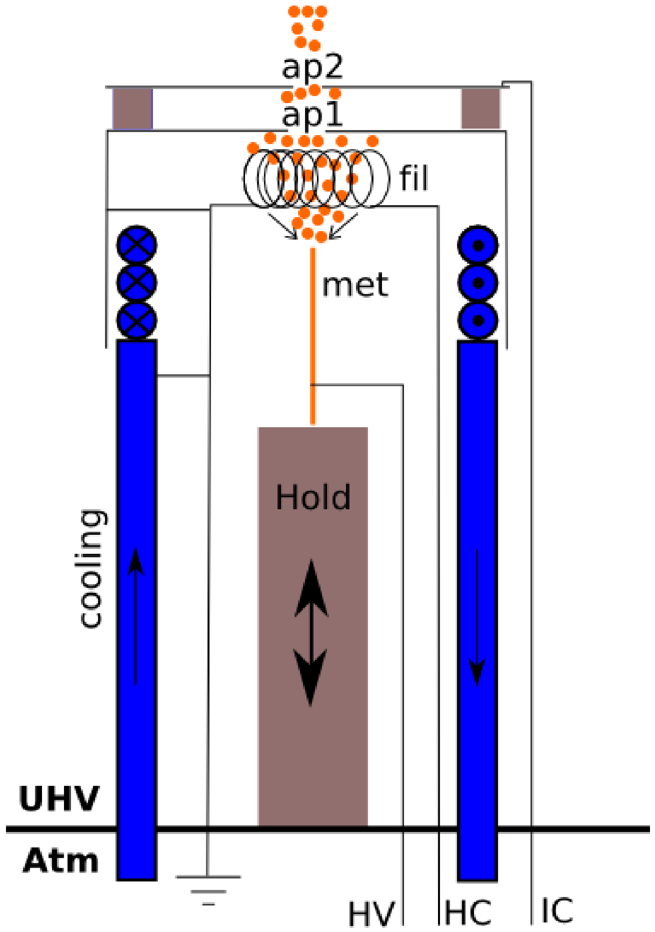

Figure 3.10: *Cross sectional diagram of evaporator used to grow metallic films. met is the high purity metal source, ap1 and ap2 are the first and second apertures, fil is a W filament, Hold is the retractable source holder, cooling is a water cooling coil, HV is a high voltage wire, HC is a high current wire, and IC is the wire carrying the ion current. Black lines are conducting, brown colouring represents insulating material, blue represents water, and orange is the source metal. The thick black line separating the UHV and Atm pressure is not in electrical contact with the HV, HC, and IC wires.*

transition from a *hcp* lattice to an *fcc* lattice, introducing disorder into the system that is visible by looking at the width of the LEED diffraction spots.

3.5.2 Ultrathin metal oxide films

The AFM ultrathin CoO film studied in this work is a metal oxide. The metal oxide ultrathin films were grown on top of an ultrathin Co film to create an AFM/FM coupled bilayer system. To produce ultrathin metal oxide films, evaporation was combined with two oxidation mechanisms: exposure growth and reactive growth. The ultrathin oxide films were grown at room temperature as at higher temperatures the Co/W(110) is more disordered and absorbed O may be rapidly diffused away from the Co(0001) surface prohibiting the formation of CoO[46].

Exposure growth is a tested way to produce ultrathin CoO films on Co [38, 46, 47, 48, 49, 50, 51, 52, 53]. To grow an ultrathin metal oxide film by exposure growth, an ultrathin metallic film is grown using evaporation prior to being oxidized by exposure to a partial O_2 pressure of $\sim 10^{-6}$ Torr. Exposure is measured in Langmuirs (L) where $1\text{ L} = 10^{-6}$ Torr s. In this work exposures ranging from 5-10000 L were used. Exposure growth will produce a bilayer film if the oxidization does not penetrate to the lowest layer of the parent film, which depends on the amount of exposure and the thickness of the parent film. The advantages of this method lie in its simplicity and the fact that the interfacial exchange interaction is greatest in exposed films [30, 53]. The main disadvantage of this oxidization method is that it is difficult to determine the thickness of the oxide layer. Because the O is absorbed from the surface and then diffuses through the lattice to lower layers of the film, the interface between the metal and metal oxide is assumed to be rough. Work by Getzlaff *et. al* [52, 54] show that at room temperature two O species, chemisorbed O and CoO, exist simultaneously for oxidized ultrathin Co/W(110) films, although at higher exposures ($>$ 100 L) CoO dominates. Both Duò *et. al* [47] and Gruyters [41] estimate a saturation thickness of 20 Å, corresponding to an exposure of $\sim 10^4$ L for a bulk Co sample. Castro and Küppers [51] estimate the depth of the oxide layer of an oxygen saturated *hcp* Co (0001) surface to be 10 Å, based on the depth of their ultraviolet photoemission spectroscopy (UPS) probe. Smardz *et. al* [55] found that when Co films of thicknesses $>$ 5 nm are exposed to atmospheric conditions, the saturated CoO oxide layer has a thickness of 25 Å. At lower temperatures ($<$ 130 K) Co_3O_4 is the oxide formed by exposure of Co films [51, 52].

Reactive growth is achieved by growing an ultrathin metallic film by evaporation, only in an elevated partial O_2 pressure. Metal and O atoms combine simultaneously with film growth, ensuring uniform distribution within the AFM film. The amount of Co deposited on the film is known from the calibration of the evaporator and can be used to estimate the film thickness. This method allows for the creation of bilayer systems with different compositions (e.g. CoO/Ag [56, 57] and CoO/Au [39]) and a sharper interface, although such an application is not evident in this work. Some exposure occurs before evaporation begins, while the O pressure is slowly raised (to ensure the pressure does not rise too much). It seems that reactive growth is the better method, but it has the experimental drawback that the filament must be heated in an O rich environment. The surfaces of the evaporator absorb a lot of O that is released in subsequent uses of the evaporator, creating a high O partial pressure local to the evaporator. This is unwanted as it contaminates the subsequent growth of pure ultrathin Co films. To remove the excess O the evaporator must be degassed several times, which is a time consuming process.

3.6 Magnetic measurements

SMOKE has become a popular method for the measurement of magnetization in ultrathin films because it can be performed *in situ*, has a linear dependence on the magnetization, and is relatively inexpensive to implement. This section will briefly explain the mechanism of SMOKE and discuss the optical system used to measure this effect.

3.6.1 Surface magneto-optic Kerr effect

SMOKE describes how the light is reflected off an ultrathin magnetic film on top of a substrate. The thickness limit for SMOKE is set by [58]:

$$\frac{2\pi}{\lambda}|N|t \ll 1 \tag{3.18}$$

where λ is the wavelength of the reflected light, N is the complex index of refraction of the film, and t is the thickness of the film. If this condition is not met, rotation of the polarization caused by the magnetization of the sample is said to be due to the magneto-optic Kerr effect (MOKE).

Linear polarized laser light will be reflected off the surface according to the Jones reflection matrix R [59]:

$$R\ \mathbf{E}_i = \begin{pmatrix} r_{ss} & r_{sp} \\ r_{ps} & r_{pp} \end{pmatrix} \begin{pmatrix} E_{is} \\ E_{ip} \end{pmatrix} = \begin{pmatrix} E_{rs} \\ E_{rp} \end{pmatrix} = \mathbf{E}_r \tag{3.19}$$

where the subscripts s and p refer to light polarized perpendicular and parallel to the scattering plane, respectively, and the subscripts i and r refer to the incident and reflected light, respectively. Light will be unchanged in polarization if R is diagonalized. The off diagonal components will be non zero if the surface possesses a net magnetization. If this is the case, r_{sp} and r_{ps} are linearly related to the off diagonal elements of the dielectric tensor ϵ_d, which can be expressed by equation 3.20 [60]:

$$\epsilon_d = N^2 \begin{pmatrix} 1 & iQ & 0 \\ -iQ & 1 & 0 \\ 0 & 0 & 1 \end{pmatrix} \tag{3.20}$$

where Q is the magneto-optic Voigt parameter. Q is proportional to the magnetization of the film; therefore, the change in polarization is also proportional to the magnetization. The change in polarization for measurement in the longitudinal orientation (magnetization parallel to plane of incidence and parallel to the film surface) and polar orientation (magnetization parallel to plane of incidence and perpendicular to the film surface) is given by the following [61]:

$$\Phi_{LON} = \sin\theta \, \frac{4\pi}{\lambda} \, \frac{N_s}{1 - N_s^2} \, Qt \tag{3.21}$$

$$\Phi_{POL} = -\cos\theta \, \frac{4\pi}{\lambda} \, \frac{N^2}{1 - N_s^2} \, Qt \tag{3.22}$$

where N_s is the complex index of refraction of the substrate. The transverse orientation (magnetization perpendicular to plane of incidence and parallel to the film surface) produces a small ($\sim 0.01\%$) change in the intensity of light that is proportional to magnetization [62]. In this work, only longitudinal SMOKE will be employed, despite the fact that we are examining the transverse susceptibility. This is because for these measurements the applied field and the change in magnetization will be transverse to the relaxed magnetization and longitudinal to the plane of incidence; in reference to figure 2.2(b) the plane of incidence is parallel to $\Delta\mathbf{M}$ and $\Delta\mathbf{H}$.

3.6.2 Optical setup

The optical system used to observe SMOKE is shown in figure 3.11. A collimated beam of light, originating from a 5 mW HeNe 632.8 nm laser (type UniPhase 1125p), passes through a Glan-Taylor polarizing prism (labelled "Polarizer" in figure 3.11), reflects from a pair of adjustment mirrors (not shown), and goes into the UHV chamber *via* a quartz window. The laser beam is reflected off of the sample at an angle of incidence of 45°. The reflected beam leaves the UHV chamber through another quartz window, and is then is polarized by the analyzer prism, a second Glan-Laser polarizing prism. A HeNe red-line 10 nm band filter is used to eliminate noise from other wavelengths of light. Finally the beam is focused onto a Si photodetector.

Performing SMOKE measurements *in situ* complicates the optical system as the laser beam must pass through two quartz windows. If these windows are stressed, their index of refraction develops a dependence on the polarization of light, a phenomenon is called birefringence. To keep UHV conditions the window must be bolted to the chamber, which causes enough stress in the quartz to cause birefringence. If the index of refraction is dependent on the polarization, a phase shift will occur because one polarization will travel through the window faster than the other, causing the linearly polarized light to become elliptical; this is illustrated in figure 3.11. Previous work in our group [63] has shown that, by tilting the polarization slightly away from *s* or *p* polarization, the birefringence of the windows can be used to negate the ellipticity

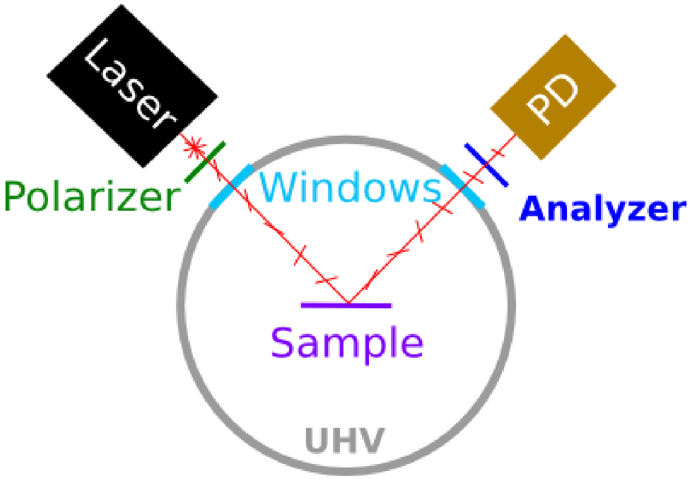

Figure 3.11: *Diagram of the optical setup used to observe SMOKE. Laser: 5 mW HeNe 632.8 nm laser. Polarizer: Glan-Taylor polarizing prism. Windows: 7 cm thick quartz windows. UHV: ultrahigh vacuum chamber. Sample: film and substrate mount of manipulator arm. Analyzer: Glan-Laser polarizing prism. PD: HeNe red-line 10 nm band filter and silicon photodetector. The laser beam is in red and its polarization is indicated by the shorter bars.*

caused by reflection from the metallic sample when the light is no longer s or p polarized. The advantage of this method is that there are no extra optical components that require alignment, such as a quarter wave plate, facilitating the achievement of high extinction and sensitivity. The disadvantage is that information of the ellipticity is lost.

3.6.3 Magnetic hysteresis measurements

Magnetic hysteresis measurements use dc magnetic fields to probe the magnetization of the sample. The optical apparatus must be optimized to achieve the sensitivity required to measure the magnetic properties of ultrathin films. Using the diagram in figure 3.11, the photodetector (PD) experiences an intensity of light, I, given by:

$$I[\theta] = I_{max}(\sin^2\theta + \epsilon) \tag{3.23}$$

where I_{max} is the maximum intensity (polarizer and analyzer have the same polarization), θ is the angle measured from cross polarization (at minimum intensity, polarizer and analyzer have $\frac{\pi}{2}$ difference in polarization), and ϵ is the extinction ratio. The extinction ratio is defined as the intensity ratio of the crossed and parallel polarizers, and indicates the quality of polarizers. The polarizers used in this work have an extinction ratio $< 10^{-6}$.

The SMOKE signal will be a small perturbation dθ of the polarization angle about the angle θ set by the analyzer. From the derivative of equation 3.23 with respects to θ:

$$\frac{\partial I}{\partial\theta} = 2I_{max}\sin\theta\cos\theta. \tag{3.24}$$

The small angle approximation gives:

$$\delta I = 2I_{max}\theta\delta\theta. \tag{3.25}$$

Combining equations 3.23 and 3.25 provides a quantity called the contrast, which is related to the signal to noise ratio:

$$\frac{\delta I}{I[\theta]} = \frac{2\theta\delta\theta}{\theta^2 + \epsilon}. \tag{3.26}$$

The contrast reaches a maximum when $\theta = \sqrt{\epsilon} \equiv \theta_{set}$. This angle can be easily found because the corresponding intensity is twice the minimum intensity according to equation 3.23:

$$I[\theta = 0] = I_{max}\epsilon \tag{3.27}$$

and

$$I[\theta = \theta_{set}] = 2I_{max}\epsilon. \tag{3.28}$$

Then the Kerr rotation of the polarization can thus be found in absolute units:

$$\Phi_{Ker} = \delta\theta = \frac{\delta I}{2I_{max}\sqrt{\epsilon}}. \tag{3.29}$$

To achieve sensitive SMOKE measurements, the extinction ratio (contrast) must be minimized (maximized), by systematically rotating the polarizer and subsequently rotating the analyzer to find the best extinction ratio.

Once the minimum extinction ratio is found the analyzer is set at twice the minimum ($\theta_{set} = \epsilon$). Now the system is ready to perform magnetic hysteresis measurements by applying a dc magnetic field either in or out of the sample plane by the Helmholtz coils (see section 3.2). The field is slowly cycled through its full range (-60 to 60 Oe) multiple times to measure the average change in intensity by the photodetector as a function of field. For best results several loops were averaged.

3.6.4 Ac susceptibility measurements

Measurements of the ac susceptibility employs the same optical apparatus used for hysteresis measurements. For these measurements an alternating magnetic field is applied by the Helmholtz coil at a frequency determined by the reference frequency of a lock-in amplifier. The signal measured by the photodetector is fed to the lock-in amplifier, which isolates intensity fluctuations at the reference frequency from the rest of the signal. The lock-in amplifier is a dual-phase amplifier that measures two different signals, one in phase with the reference signal and the other out of phase by $\frac{\pi}{2}$. The in phase and out of phase components correspond to the real and imaginary parts of the complex susceptibility, as mentioned in section 2.5.1.

For optimal susceptibility measurements the analyzer angle θ_{set} is not simply related to the extinction ratio because frequency dependent signal-to-noise issues become significant [64]. The analyzer angle used in this work is $\theta_{set} =$ 24 arcminutes, which gives the best signal to noise ratio [65].

The Kerr rotation is found by converting the intensity measurements by the photodetector using equation 3.29. The magnetization is proportional to Φ_{Ker}; therefore, the susceptibility is also directly related to Φ_{Ker}. In absolute optical units the susceptibility is given by:

$$\chi = \frac{\Phi_{Ker}}{H_o} = \frac{\delta I(\theta_{set}^2 + \epsilon)}{2\theta_{set} I[\theta_{set}] H_o} \tag{3.30}$$

where H_o is the applied field, equations 3.23 and 3.29 have been used to eliminate I_{max} from the right side of the equation, and $I(\theta_{set})$ is the instantaneous dc intensity. To put this in cgs units a conversion factor relating the magnetization to the Kerr rotation is needed,

$$\chi = \frac{M_s}{\Theta_K t} \frac{\delta I(\theta_{set}^2 + \epsilon)}{2\theta_{set} I[\theta_{set}] H_o}, \tag{3.31}$$

where M_s is the bulk saturation magnetization, Θ_K is the Kerr rotation per saturated monolayer, and t is the thickness of the monolayer. M_s for bulk Co is 1450 $\frac{\text{emu}}{\text{cm}^3}$. Θ_K is in detail a complicated function of the optical properties of the band structure. In ultrathin films, this can depend sensitively on the film structure and strain; therefore, Θ_K must be calibrated experimentally from a hysteresis loop.

A phase shift occurs between the reference frequency of the lock-in amplifier and the signal from the photodiode. The capacitance and inductance of the field coils and various electrical components of the measuring system cause the phase shift. To put the in (x) and out (y) of phase components into real, $Re(\chi)$, and imaginary, $Im(\chi)$, parts of the susceptibility, the phase shift is corrected by a rotation matrix:

$$\begin{pmatrix} \cos\phi & -\sin\phi \\ \sin\phi & \cos\phi \end{pmatrix} \begin{pmatrix} x \\ y \end{pmatrix} = \begin{pmatrix} Re(\chi) \\ Im(\chi) \end{pmatrix} \tag{3.32}$$

where ϕ is the phase difference. The phase shift for the system used in this work has previously been reported to be 135° [65]. Small adjustments are made to ensure accuracy; for example, the measured susceptibility is prevented from passing through zero.

The ac susceptibility is usually measured as a function of temperature, although this work also examines the susceptibility *versus* applied field. This method is ideal for the detection of magnetic phase transitions and can be used to find the order of a transition.

3.6.5 Ground loops

In this work the susceptibility of an ultrathin Co film is measured far below T_C, where size of the susceptibility is small and stays relatively constant with temperature, making it hard to differentiate from a constant background signal for a linear χ. The magnetization will be linear with the applied field (for small fields). Any offset that scales with field is troublesome to eliminate. Because a lock-in technique is used, noise must occur near the reference frequency; therefore, noise must come through radio frequency (RF) interference or ground loops. RF interference is minimized by using coaxial cables and spacing various components away from each other.

Ground loops occur when two or more separate points on a circuit are at different potentials even though they are all supposedly grounded. A circuit that has two grounded points, $G1$ and $G2$, will have a ground loop if $V_{G1} \neq V_{G2}$. In the case that $V_{G1} > V_{G2}$, $G1$ can be considered to be connected to G2 through a resistor (R_G); therefore, current will flow from $G1$ to $G2$ through R_G in parallel with the rest of the circuit, causing unwanted current in the circuit.

A high current audio amplifier used to provide alternating current to the Helmholtz coils was creating a ground loop with the lock-in amplifier and the photodetector. The photodetector is grounded to the metal casing that encapsulates it, which was bolted on to the UHV chamber such that an electrical connection was formed. The UHV chamber acts as a ground for many devices used in the lab, and was somehow connected to the ground of the audio amplifier creating noise at the reference frequency. To stop the noise the connection between the photodetector and the UHV chamber was broken by using a rubber spacer and nylon bolts, isolating the photodetector from any stray currents in the UHV chamber. The audio amplifier was put on a separate ground circuit from the rest of the system to relieve the ground circuit of the system from the high current of the audio amplifier. This helped reduce the noise, even though using different grounds is a common source of ground loops, which is most likely the cause of the remaining noise.

The noise is measured by taking measurements with the laser beam blocked or turned off, so that any signal registered by the lock-in amplifier is due to noise. Before the alterations to the system to reduce the effects of ground loops, the noise was 2.5×10^{-6} V, compared to 0.58×10^{-6} V after the modifications for an applied field of 10 Oe; the equivalent Kerr rotations are 27.6 nrad and 5.5 nrad, respectively. The remaining noise is removed from the signal by subtracting the blocked signal that is completely due to noise.

Chapter 4

Results and Discussion

The results of the experiments performed in this work are presented and discussed in this chapter. The first section will cover the structural and magnetic properties of ultrathin Co/W(110) films, including calculations of the in-plane anisotropy, which will be compared to estimated values by Fritzsche *et. al* [1]. The second section will provide a comparison of ultrathin CoO/Co/W(110) films produced by exposure and reactive growth. Experimental observations showing the Néel transition *via* the interfacial exchange coupling between AFM CoO and FM Co layers will also be discussed.

4.1 Ultrathin Co/W(110) films

4.1.1 Structure of ultrathin Co/W(110) films

In section 3.3 AES is used to obtain the growth rate of Co, which was 105 s/ML, by measuring the attenuation of the W spectrum from 150 to 190 eV. A peak in the Auger spectrum shown in figure 4.1 at 778 eV corresponds to a LMM transition in Co, confirming that Co is deposited on the sample. The sample was determined to be free of contaminants, such as C and O, *via* AES detection. The growth mode of ultrathin Co/W(110) films was determined by AES to be a SK growth mode in section 3.3 as well. This is supported by Pratzer and Elmers's [66, 67] detailed scanning tunnelling microscopy (STM) and scanning tunnelling spectroscopy (STS) work that found that a pseudomorphic (ps) monolayer forms at a coverage of about 0.7 ML after annealing to 635 K. Above this coverage the initial monolayer become close-packed, with subsequent layers being bulk-like and growing in the SK growth mode [25, 66]. Johnson *et. al* [68] also report the existence of a ps monolayer and achieve the FvdM growth mode (see section 3.3) by growing with a substrate temperature of 100 K. In the present study, the LEED pattern of a 1 ML Co/W(110) film matches the 8x1 LEED pattern of a close-packed monolayer reported by Pratzer and Elmers [67]; therefore, the kink in the uptake curve in figure 3.6 corresponds to the completion of a close-packed monolayer. At steps between a monolayer and a double layer, smaller *fcc* and *hcp* triple layers form, but triple layer islands that form on top of a double layer away from steps are all *hcp* [66]. The majority of the triple layer islands are *hcp* and were determined to be thermodynamically more favourable. Knowing that the *hcp* packing is preferable is important when considering the magnetocrystalline anisotropy, as it is weaker in the *fcc* packing.

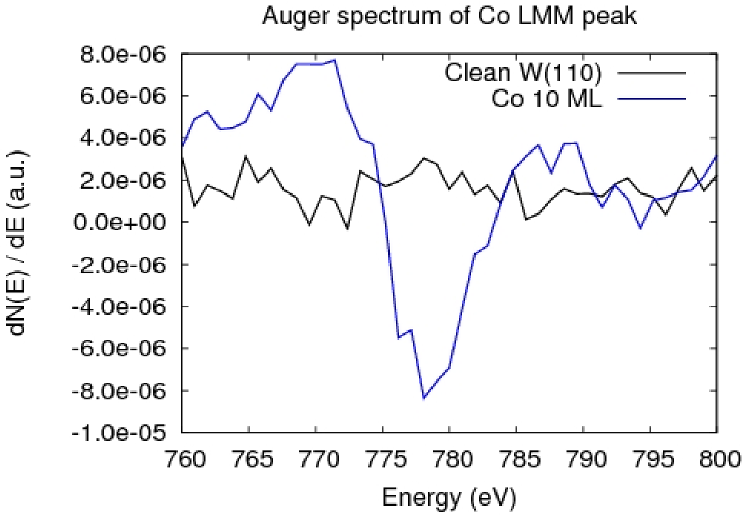

Figure 4.1: *The 778 eV AES peak of a 10 ML Co film (blue). AES spectrum of the W(110) surface (black).*

LEED was used to determine the properties of the lattice. Figure 4.2 shows the LEED pattern for ultrathin Co films of different thicknesses and comparable energies. In figure 4.2(a) the diffraction pattern of a 1 ML Co/W(110) film is shown. The diffraction spots due to the W(110) surface and ultrathin Co film are circled in green and red, respectively. The W(110) spots are still visible as LEED is sensitive to the top 3-4 ML. At 3 ML of coverage the

Co LEED spots are more intense than the W(110) spots (as shown in figure 4.2(b)). Once the coverage reaches 5 ML the W(110) LEED pattern is no longer visible. The LEED pattern of a 10 ML Co film is shown in figure 4.2(c). Using the diffraction pattern with equation 3.15, the hexagonal lattice spacing is determined to be 2.6 ± 0.1 Å, which is consistent with the bulk hexagonal lattice parameter of 2.51 Å. The length of the reciprocal lattice vector is found by averaging the measurements from the diffraction pattern of the distance from the centre spot to the six spots of the hexagonal pattern and the distance between neighbouring spots on the hexagonal pattern; the error is given by the standard deviation of this set of values.

The arrows in figure 4.2(b) indicate the crystallographic directions of the W substrate. The [0001] or fcc [111] direction of the ultrathin Co film is parallel to the [110] direction of the W substrate, which is called the Nishiyama-Wassermann orientation [23, 24, 25]. The LEED spots have a similar spacing along $[1\bar{1}0]$ for the W and Co surface, yet are significantly different along the [001] direction, corresponding to lattice mismatch in real space. The lattice mismatch along the [001] direction is 20.5% as predicted in section 2.4.5. The narrow LEED spots (similar width to those of the W(110) substrate) are indicative of long range order within the film [25].

The inter-planar spacing of Co was found by observing the intensity of the central LEED spot using the method described in section 3.4. Figure 4.3(a) is a graph of the LEED intensity maxima energies *versus* diffraction order squared.

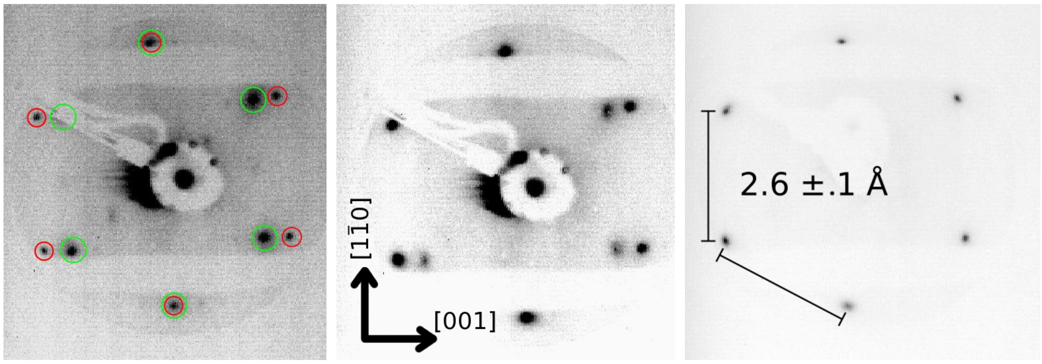

(a) (b) (c)

Figure 4.2: *LEED patterns of ultrathin Co films on W(110): a) 1 ML with incident beam energy,* $E_B = 89.1$ *eV; b) 3 ML,* $E_B = 88.0$ *eV; c) 10 ML,* $E_B = 91.6$ *eV. In a) spots due to the W lattice are circled in green and spots due to the Co lattice are circled in red. In b) the crystallographic directions of W(110) in reciprocal space are given, which are the same in all LEED images. In c) the hexagonal basal lattice constant corresponding to the reciprocal lattice vectors is given.*

The inter-planar spacing is found to be 2.02 ± 0.09 Å, which is consistent with the bulk value of 2.035 Å. The inter-planar spacing corresponds to half of the c lattice parameter of the standard *hcp* unit cell, as each cell has atoms in the A and B oriented planes. The order of diffraction of the first observed peak, n_o, was determined by minimizing the mean squares difference of a linear fit of the resonant energies *versus* diffraction order squared.

Lattice parameters of ultrathin films and bulk materials can differ by $<$ 10% in length; therefore, it can be useful to calculate a set of bulk resonant energies using the Bragg condition to serve as an assessment of the selection of n_o. As the spacing is similar the variance between energies should be small for reasonable selections of n_o. The variance between the expected and measured resonance energies is given by:

$$\sigma_E = \frac{1}{N} \sum_{n=0}^{N-1} (E'_n - E^{Co}_{n_o+n})^2 \tag{4.1}$$

where N is the total number of diffraction points observed, E'_n is the observed energy of the n^{th} LEED intensity maxima minus an offset energy to account for the work functions of the filament and the film, and E^{Co}_n is the n^{th} expected resonance energy of bulk Co, which varied greatly for different values of n_o. The offset was determined by fitting the data to the expected energy series. The variance is plotted as a function of n_o in figure 4.3(b), indicating that it is reasonable for n_o to be the second order of diffraction as this corresponds to a minimum in the variance. This is in accordance with the linear fitting.

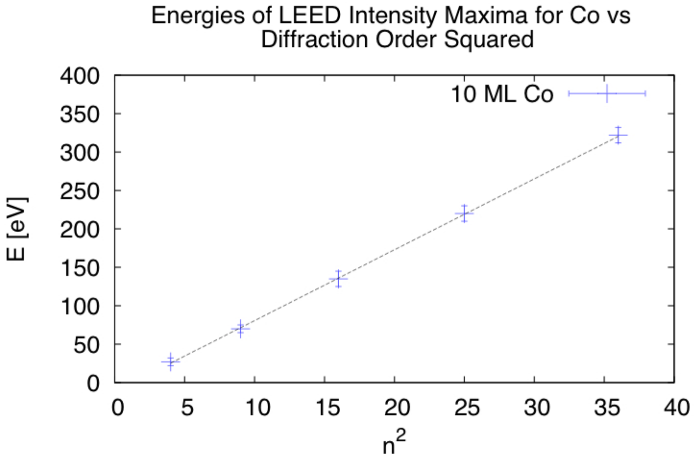

(a)

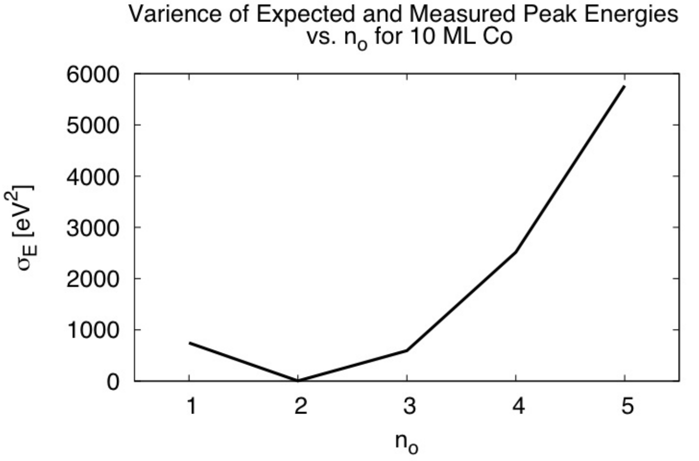

(b)

Figure 4.3: *LEED analysis of a 10 ML Co/W(110) film. a) Plot of the energies of the central LEED spot intensity maxima* versus *diffraction order. The slope of this graph corresponds to an inter-planar spacing of* 2.02 ± 0.09 *Å. b) Plot of the variance between the expected and measured resonance energies* versus n_o.

4.1.2 Hysteresis measurements

Magnetic hysteresis measurements of FM ultrathin Co/W(110) films are presented in figure 4.4. A single 10 ML Co sample is shown in figures 4.4(a), 4.4(b), and 4.4(c). It was annealed at 400 K for 150 s. The hysteresis loop with field directed along the $1\bar{1}0$ axis in figure 4.4(a) indicates magnetic reversal. The square shape of the loop suggests that the magnetization is flipped due to the motion of a domain wall across the probing area and that the height of the loop equals twice the saturation signal. A field of 50 Oe is required to flip the magnetization by π. The magnetization prefers to lie on the $1\bar{1}0$ axis, identifying it as the easy axis. In figure 4.4(b) the dc field is applied along the hard 001 axis. The slight slope corresponds to the magnetization being tilted away from the easy axis by the applied field; the line of best fit (shown in red) has a slope of $0.09 \pm 0.01\ \frac{\mu\mathrm{rad}}{\mathrm{Oe}}$. In figure 4.4(c) the applied dc magnetic field is out of the plane of the sample. No sizeable dc signal is present. The hysteresis loop of a 20 ML Co/W(110) film is presented in figure 4.4(d). This loop is significantly less noisy because a smaller gain was used on the photodetector.

Hysteresis loops were obtained for only two of eight samples. This is because dc measurements require superior optical alignment compared to ac measurements that use lock-in detection. The height of the hysteresis loop is needed for the determination of the anisotropy as the value of M_s is taken as half of the height of the loop. The Kerr rotation, assuming saturation magnetization, is found to be $2.0 \pm 0.5\ \frac{\mu\mathrm{rad}}{\mathrm{ML}}$ for the 10 ML film and $0.9 \pm 0.1\ \frac{\mu\mathrm{rad}}{\mathrm{ML}}$ for the 20 ML film. Partial pinning of domain walls in the probing area, as well as a nonlinear relationship between the saturation magnetization and film thickness, is responsible for the disparity between the 10 ML and 20 ML results. Oepen *et. al* [69, 70] obtained a saturation Kerr rotation of $19.5 \pm 0.5\ \frac{\mu\text{rad}}{\text{ML}}$ for ultrathin Co/Cu(001) films and $16.5 \pm 1\ \frac{\mu\text{rad}}{\text{ML}}$ for ultrathin Co/Cu(1117) films, which are both an order of magnitude greater than values found in this work.

4.1.3 Transverse susceptibility measurements

To test the SMOKE system's ability to detect a small rotation of the magnetization by a transverse field (see figure 2.2(b)), the Kerr rotation was measured as a function of the applied transverse field strength. Figure 4.5 shows the result of this experiment using the raw data acquired from the photodetector. This is an important result as the susceptibility relation in equation 3.31 is only valid when the magnetization increases linearly with applied field. This condition holds for fields of at least 10 Oe, which is the maximum field produced by our amplifier. Susceptibility measurements in the rest of this work used an applied field of 10 Oe as the larger field provides a greater signal.

As mention in section 3.6.5, remaining ground loop noise must be removed by subtracting blocked measurements, which are photodetector measurements taken when a field is applied and the laser beam is blocked by a beam stop. There is still an offset in the photodetector output that is independent of the applied field; a zero field measurement thus sets the zero ac magnetization.

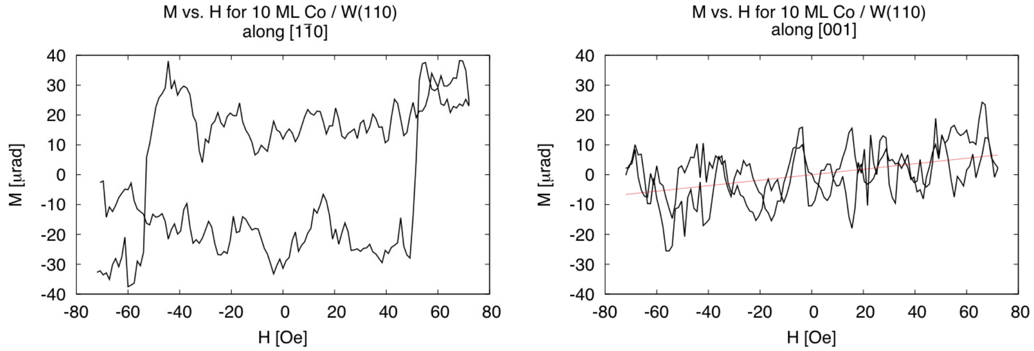

(a) In-plane longitudinal (b) In-plane transverse

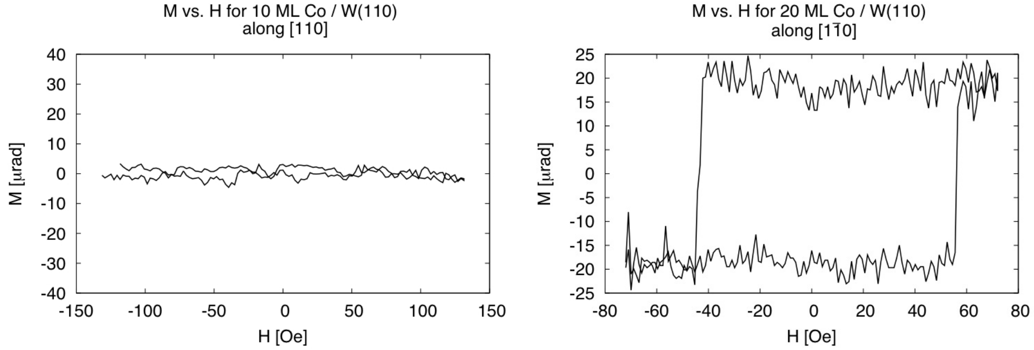

(c) Out of plane transverse (d) 20 ML, In-plane longitudinal, Sample C

Figure 4.4: *Plots of hysteresis measurements of 10 ML (a-c) and 20 ML (d) Co/W(110) films with field applied in the: a), d)* [1$\bar{1}$0] *direction; b)* [001] *direction; c)* [110] *direction.*

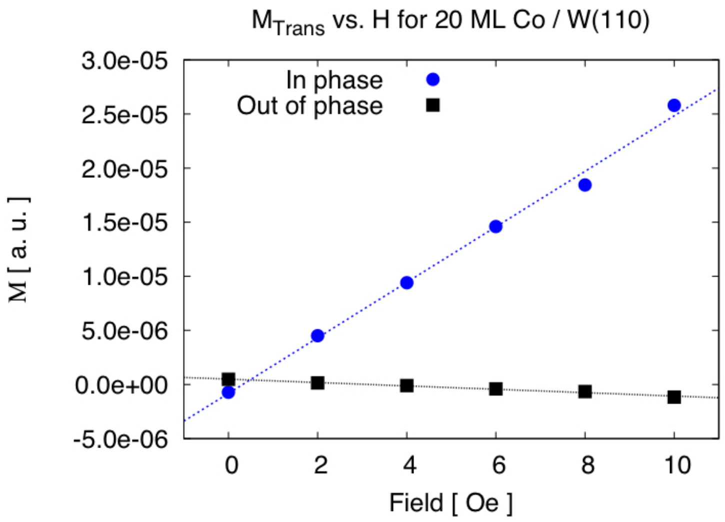

Figure 4.5: *Plot of transverse magnetization* versus *applied field for a 20 ML Co film. The magnetization is measured in V, which is the form of the raw data from the photodetector.*

The transverse susceptibility of ultrathin Co/W(110) films was measured as a function of temperature in order to evaluate the magnetic anisotropy using the method outlined in this work and to serve as a comparison for the susceptibility of coupled ultrathin CoO/Co/W(110) films. The films were magnetized along the easy axis by performing dc magnetic measurements that apply large fields. The zero field and blocked transverse measurements are made before zero field cooling below 150 K. Field cooling is not possible as running a dc field for an extended period of time causes the Helmholtz coils to overheat. Once cooled, the zero field and blocked transverse measurements are then made again to verify consistency at low temperatures. Transverse susceptibility measurements are made as the sample is being heated radiatively at a rate of 0.02 K/s, so that data can be binned. The data is put into bins of ~ 1 K; each bin has an average value of ~ 90 points. The in phase and out of phase parts of the blocked susceptibility measurement (accounts for noise in the system) and the zero field susceptibility measurement (taken as the true zero Kerr rotation) are subtracted from their corresponding parts from the susceptibility signal. Equation 3.30 is then used to convert the signal to optical units and the phase is adjusted using a rotation matrix.

The number of samples in this study was limited by the amount of time required to perform the experiments, which each took at least 24 h of attentive supervision. The slow rate of heating (0.02 K/s) means that susceptibility measurements can take up to 2.75 h, plus 1-2 h to cool the sample. This must be performed twice, before and after oxidation. Oxidation and the warming of filaments are lengthy procedures as well.

Figure 4.6 shows the susceptibility of three different 20 ML Co/W(110) films. The imaginary part of the susceptibility has been enlarged five times for clarity. All samples are fabricated the same way. Numerous factors, such as contamination due to residual O_2 gas and out gassing of the evaporator's casing or filament, may explain the difference in the measured susceptibilities. Sample A is free of obvious defects and represents the expected form of the Co transverse susceptibility: the real component increases linearly with increasing thermal energy and the imaginary component is featureless. Sample B has a

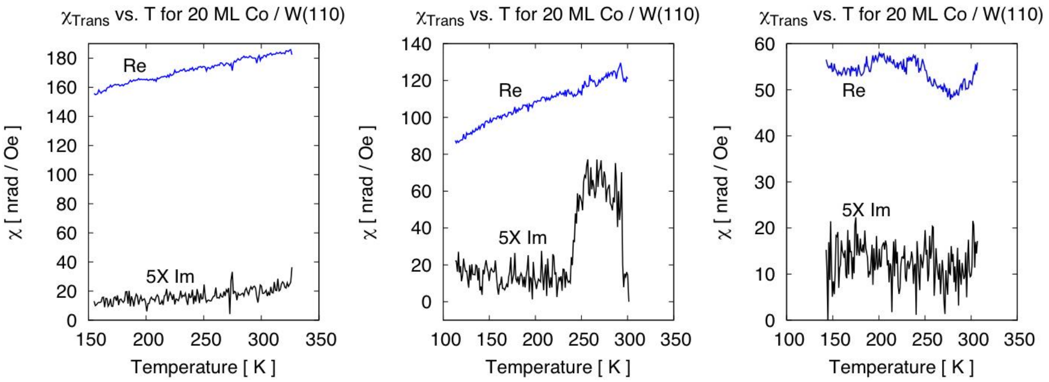

(a) Sample A (b) Sample B (c) Sample C

Figure 4.6: *Plots of transverse susceptibility of ultrathin Co/W(110) films* versus *temperature.*

non-reproducible jump in the imaginary component at ∼ 230 K and then a jump back at ∼ 290 K, which may be caused by accidental movement of the optics or electrical wires when refilling the liquid nitrogen reservoir. Sample C has an irregular form in its real part that decreases with temperature. To quantify the temperature dependence of the transverse susceptibility, the real part of the susceptibility was fitted to a straight line. The fitting parameters for the 20 ML Co film in figure 4.6 are presented in table 4.1. The transverse susceptibility of a 10 ML Co/W(110) film was found to be $45 \pm 3 \ \frac{\mathrm{nrad}}{\mathrm{Oe}}$ at room temperature.

Sample	Slope $[\frac{\text{nrad}}{\text{Oe K}}]$	Intercept $[\frac{\text{nrad}}{\text{Oe}}]$	Variance $[\frac{\text{nrad}^2}{\text{Oe}^2}]$
A	0.162 ± 0.002	132.6 ± 0.5	1.6
B	0.196 ± 0.003	67.5 ± 0.6	4.1
C	-0.029 ± 0.003	60.5 ± 0.8	4.5

Table 4.1: *Linear fit coefficients of the transverse susceptibility (samples A, B, and C) with increasing temperature.*

4.1.4 Determination of anisotropy

The anisotropy field, $\mathbf{H}_{aniso}$, of the ultrathin Co film can be found using equation 2.30, provided accurate measurements are made of the transverse susceptibility and the saturation magnetization. The derivation of $\mathbf{H}_{aniso}$ of sample C at room temperature is given as an example:

$$\mathbf{H}_{aniso} = \frac{\mathbf{M}_s}{\chi_{trans}} = \frac{18\ \mu\text{rad}}{51\ \text{nrad/Oe}} = 350\ \text{Oe} \tag{4.2}$$

where χ_{trans} is the transverse susceptibility that was discussed in the previous section. The anisotropy field is calculated using optical units as this avoids estimating the saturated magnetization. The Kerr rotation corresponding to $\mathbf{M}_s$ is found from the longitudinal hysteresis loops presented in figure 4.4. A hysteresis loop belonging to sample C is presented in figure 4.4(d), and gives a saturated Kerr rotation of 18±2 μrad. Unfortunately this is the only hysteresis loop obtained in this work for a 20 ML Co/W(110) film. Accordingly, the anisotropy fields of all of the 20 ML samples are calculated using the saturated

Kerr rotation of sample C. Figure 4.7 presents the anisotropy field as a function of temperature. The error bars are representative of the uncertainty in the saturated Kerr rotation. In samples A and B the anisotropy field decreases with temperature, showing that increasing thermal energy decreases the effect of the anisotropy.

Equation 2.29 is only valid if the small angle approximation is applicable to the angle ψ in figure 2.4 ($\psi < 10°$). Any error incurred by the small angle approximation used in equation 2.29 should be much smaller than the relative error of $\mathbf{M}_s$, which is $\sim 10\%$. For an applied field of 10 Oe, the error in the small angle approximation is $\sim 1\%$ for sample A and smaller for samples B and C. This is acceptable as $\sim 1\%$ is an order of magnitude smaller than the relative uncertainty in $\mathbf{M}_s$.

The saturated Kerr rotation for a 10 ML Co/W(110) film was found to be 20 ± 4 μrad, which is half the height of the hysteresis loop in figure 4.4(a). Using the transverse susceptibility of 45 ± 3 $\frac{\text{nrad}}{\text{Oe}}$, the anisotropy field is found to be 400 ± 100 Oe.

According to equation 2.26 a factor of $M_s/2$ is needed to express the anisotropy fields in terms of energy density. Assuming the films are saturated, M_s for Co is 1450 $\frac{\text{emu}}{\text{cm}^3}$. To compare this work with the anisotropy energy densities measured by Fritzsche *et. al* [1], the results must be converted to SI units using a factor of $10\ \frac{\text{erg}}{\text{cm}^3} = 1\ \frac{\text{J}}{\text{m}^3}$. The anisotropy energy densities at room temperature are presented in table 4.2.

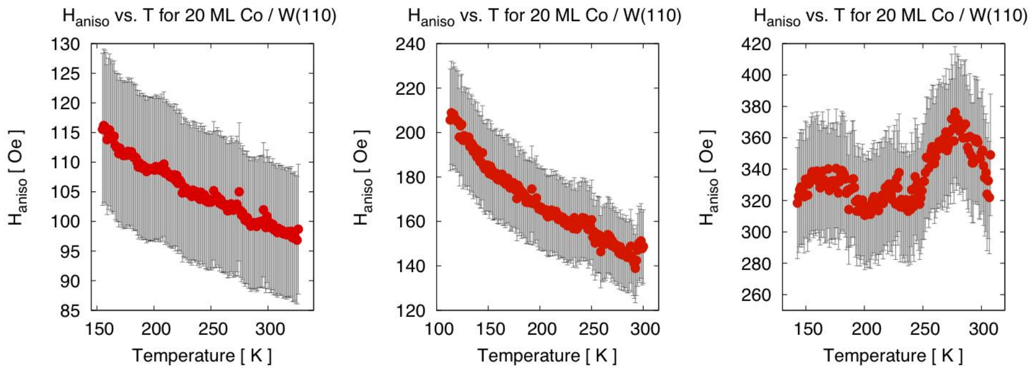

(a) Sample A (b) Sample B (c) Sample C

Figure 4.7: *Plots of anisotropy fields of ultrathin Co/W(110) films* versus *temperature.*

The anisotropy for the 10 ML sample can also be found using the hysteresis loop in figure 4.4(a) and the slope from figure 4.4(b). The slope is the transverse susceptibility as it measures the change in the transverse magnetization with applied field. Using equation 2.30, the anisotropy field is found to be 220 ± 60 Oe. This method is not as accurate because it is a dc technique that accepts noise of all frequencies; however, it does produce an energy density of the same order of magnitude as that found by a combination of ac and dc techniques.

Fritzsche *et. al* [1] plot the anisotropy energy density multiplied by the film thickness in order to separate the volume and surface contributions of the total anisotropy energy density. The unit cell parameters from their LEED results give a thickness of 0.20 ± 0.01 nm/ML, which agrees with the present

Sample	Anisotropy Field	Anisotropy Energy Density	
Co	[Oe]	cgs $[10^5 \frac{\mathrm{erg}}{\mathrm{cm}^3}]$	SI $[10^4 \frac{\mathrm{J}}{\mathrm{m}^3}]$
10 ML	400 ± 100	3 ± 0.7	3 ± 0.7
20 ML A	100 ± 10	0.73 ± 0.07	0.73 ± 0.07
20 ML B	150 ± 20	1.1 ± 0.1	1.1 ± 0.1
20 ML C	350 ± 40	2.5 ± 0.3	2.5 ± 0.3

Table 4.2: *Anisotropy energy densities for 10 ML and 20 ML (samples A, B, and C) Co/W(110) films at room temperature. The values from sample C were derived from one experiment where both the transverse susceptibility and a hysteresis loop were measured on the same film.*

work. The anisotropy energy densities in table 4.2 are overlaid on the data from Fritzsche *et. al* [1] in figure 4.8. The product of the energy density and the film thickness is expressed as the free energy per area on the y axis. The data from this work is denoted by coloured diamonds: the 10 ML sample is in red, and samples A, B, and C are in blue, orange, and green, respectively. Sample C is highlighted with an "x" because it is the only sample where both the transverse susceptibility and a hysteresis loop were obtained. The results from this work produce anisotropy energy densities an order of magnitude smaller than that of the bulk ($K_2 = 5.28 \times 10^6 \ \frac{\mathrm{erg}}{\mathrm{cm}^3}$) and close to an eighth of what has previously been reported by Fritzsche *et. al* [1] in the cases of the 10 ML sample and sample C.

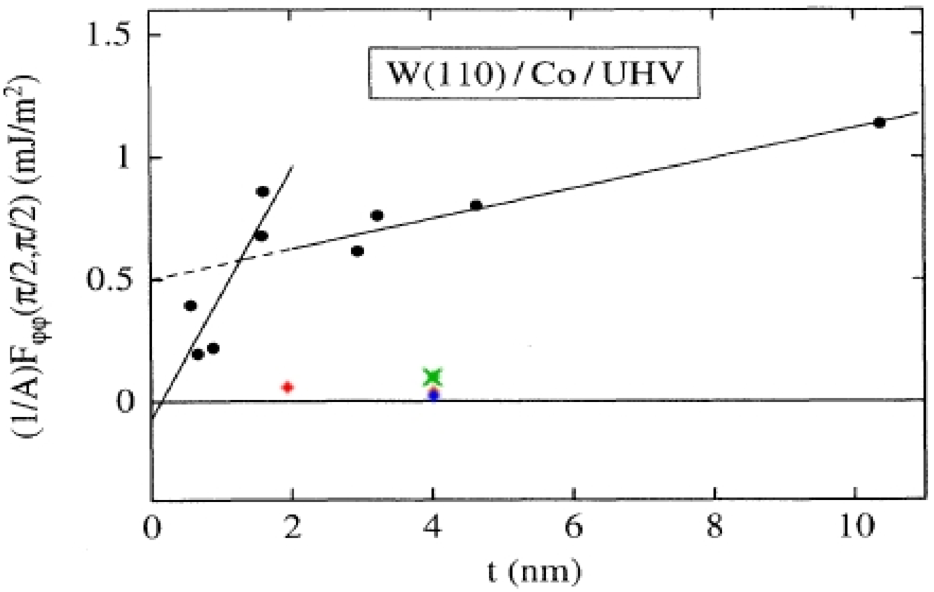

Figure 4.8: *Plot of film thickness multiplied by anisotropy energy density* versus *film thickness from [1], with data from this work overlaid: 10 ML sample is in red, and samples A, B, and C are in blue, orange, and green, respectively. Sample C is highlighted with an "x" because it is the only sample for which the transverse susceptibility and a hysteresis loop were obtained. The energy density multiplied by the film thickness is expressed as the free energy per area.*

Disagreement between these results is not surprising considering that the magnetic anisotropy is sample dependent. De Jonge *et. al* [3] tabulated anisotropy measurements of ultrathin Co films grown on different substrates. They showed that the surface anisotropy constant, K_s, of ultrathin Co/Pd(111) films can vary by a factor of 5.8 and that the volume anisotropy constant, K_v, can vary by a factor of 2.4. K_s and K_v are the intercept and slope, respectively, of a straight line on a graph of film thickness multiplied by anisotropy energy density *versus* film thickness (see section 2.4 and figure 4.8). Variation in the measurement of the anisotropy constants commonly occurs for ultrathin Co film systems; therefore, is not completely unreasonable for the anisotropy energy densities to differ by a factor of eight.

An inaccurate value of the saturated Kerr rotation could be the source of the discrepancy between the results in this work and those of Fritzsche *et. al* [1]. Oepen *et. al* [69, 70] found a saturated Kerr rotation an order of magnitude greater for ultrathin Co/Cu(001) and Co/Cu(1117) films than what is reported here. A difference in the saturation Kerr rotation is expected for various substrates as the band structure within the film will differ; however, the large disparity suggests that the magnetization is not saturated and that the observed hysteresis loop is due to domain wall motion in a fraction of the probing area. If domain pinning creates an energy barrier that is greater than the magnetic energy supplied by the applied field, the magnetic domain structure is frozen. To achieve saturation magnetization a larger applied field is needed. Domain pinning does not affect the transverse susceptibility when all the domains in the probing area are magnetized along one of the directions of the easy axis because the measured magnetization is perpendicular to the easy axis. If two antiparallel magnetic domains are subject to a transverse field, their magnetization will be tilted in the same direction, thus having an additive effect on the transverse magnetization. The inconsistency of the appearance of hysteresis loops is consistent with domain pinning because, if all of the domains within the probing area are pinned, a hysteresis loop would not be observed. The same domain pinning argument could also explain the large variation in the saturation Kerr rotation per monolayer between the 10 ML and 20 ML samples.

Pinning is not the only reason the saturated Kerr rotation per monolayer would be smaller than expected; it would differ for thicker films because the rate at which the anisotropy increases changes at a critical thickness. As mentioned in section 2.4.5, Fritzsche *et. al* [1] have identified the coherent and incoherent regimes. The data in this work lie in the incoherent regime; therefore, the saturated Kerr rotation per monolayer is expected to be smaller than in a film in the coherent regime because of the kink in anisotropy *versus* thickness curve. It is difficult to say whether the small saturation Kerr rotation per monolayer is accurate without further dc measurements with higher magnetic fields.

The reduction in ground loop noise allowed the transverse susceptibility of ultrathin Co films to be measured distinct from any critical transitions. A novel technique that uses ac susceptibility measurements and dc hysteresis measurements was employed to determine the anisotropy energy density. Although the results are reasonable, they are about a factor of eight smaller than what was predicted by Fritzsche *et. al* [1]. Both the ac and dc magnetic measurements contain inconsistencies; therefore, more samples are necessary to arrive at a definitive value of the anisotropy energy density.

4.2 Ultrathin CoO/Co/W(110) films

In this section the properties of ultrathin CoO/Co/W(110) films produced by two different methods, exposure growth and reactive growth, will be compared using AES and LEED. The transverse susceptibility of ultrathin CoO/Co/W(110) exposure growth films is presented as proof of observation of the Néel transition.

4.2.1 AES of ultrathin CoO/Co/W(110) films

AES cannot be used to determine the growth rate of the CoO layer for exposure growth and reactive growth because the Co spectrum of the Co base layer is indistinguishable from that of the Co atoms in the CoO layer; however, AES still provides valuable information on the constituents of the film. Typical Auger spectra of both growth methods are presented in figure 4.9. The three

KLL peaks of O are present between 460 eV and 530 eV, and a LMM peak of Co is observable between 760 eV and 800 eV. Both methods yield similar spectra varying only slightly in amplitude. AES is almost equally sensitive to O and Co; therefore, the surface is composed of O as the size of the largest O KLL is greater than twice that of the Co LMM signal.

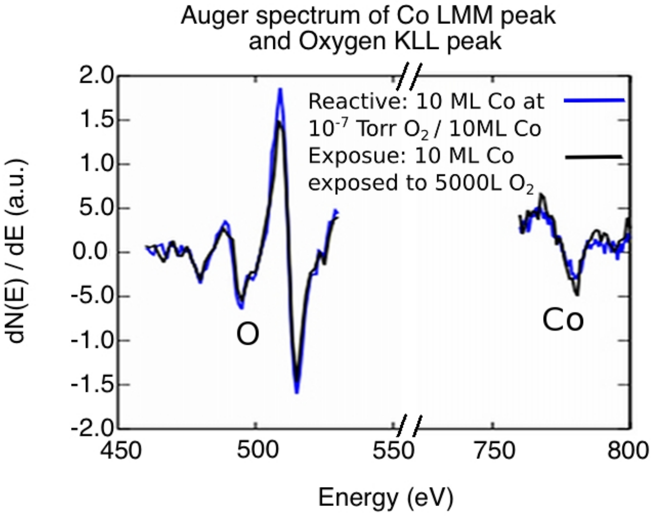

Figure 4.9: *Auger spectra for ultrathin CoO films grown by exposure and reactive growth. Peaks at energies ranging from 460 to 530 eV correspond to the O KLL peaks. Peaks at energies ranging from 760 to 800 eV correspond to the Co LMM peaks.*

4.2.2 LEED of ultrathin CoO/Co/W(110) films

LEED patterns for exposure and reactive growth methods produce similar results. Figure 4.10 is a collection of LEED patterns of 10 ML Co/W(110) films for different amounts of O_2 exposure. The incident beam energy, amount of exposure, and associated lattice spacing are given below each image. The LEED pattern is independent of the amount of exposure over the range of 5-5000 L, indicating that the top layers of the Co film oxidize after only 5 L of exposure. Figure 4.10(d) includes bars indicating the lattice vectors used to calculate the in-plane lattice spacing, which on average was found to be 3.0 ± 0.1 Å.

The LEED images for reactive growth samples are presented in figure 4.11. The incident beam energy, equivalent Co thickness, O_2 pressure during growth, amount of O_2 exposure, and associated lattice spacing are given below each image. The results for reactive growth samples produced in pressures of 10^{-8} and 10^{-9} Torr have been omitted because O desorbing from within the evaporator created a higher local O pressure than what was read by the ion gauge. Again, there is little variation in the LEED patterns.

The LEED images show that both growth methods produce films with hexagonally packed surfaces and an in-plane lattice spacing of 3.0 ± 0.1 Å, which agrees with the 3.012 Å bulk lattice spacing of CoO. The diffuse diffraction spots are characteristic of a polycrystalline sample with the crystallites maintaining preferential orientation. Lee *et. al*, in their study of the oxidation of the Co(0001) surface [71], claim that oxidation initially forms islands of CoO that increase in depth and girth with increasing O_2 exposure to eventually coalesce and fully cover the Co(0001) surface. The oxide film is in-

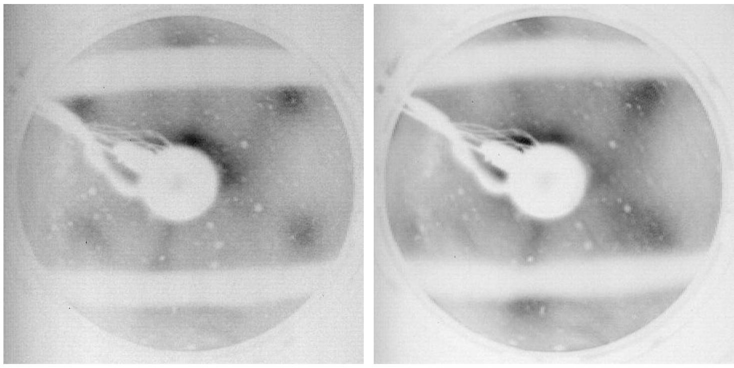

(a) 78.6 eV, 5 L, 3.1 ± 0.1Å (b) 66.0 eV, 50 L, 2.9 ± 0.1Å

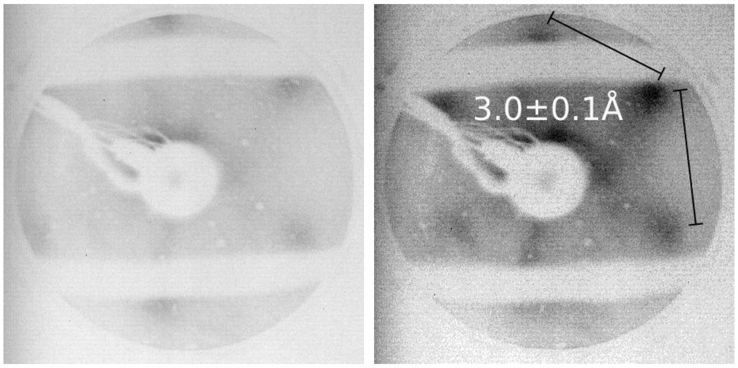

(c) 61.8 eV, 550 L, 3.0 ± 0.1Å (d) 88.0 eV, 5,000 L, 3.0±0.1Å

Figure 4.10: *LEED images of ultrathin CoO/Co/W(110) exposure growth films. The incident beam energy, amount of O_2 exposure, and the hexagonal lattice spacing for each sample are provided below the images. All samples had a Co film thickness of 10 ML. In d), reciprocal lattice vectors used to determine lattice spacing are drawn.*

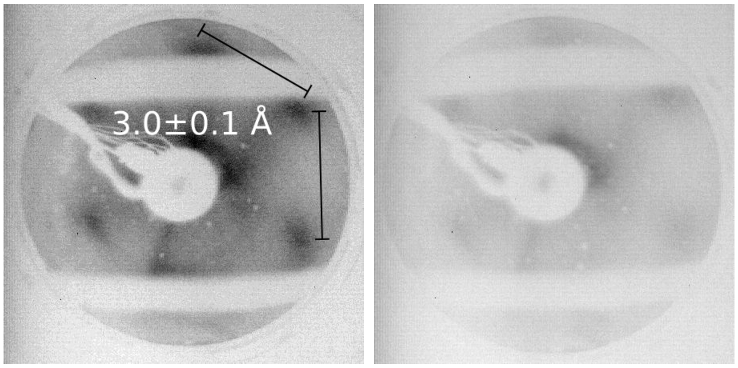

(a) 88.7 eV, 5 ML, 10^{-7} Torr, 52 L, 3.0 ± 0.1Å

(b) 84.0 eV, 10 ML, 10^{-7} Torr, 105 L, 3.0 ± 0.1Å

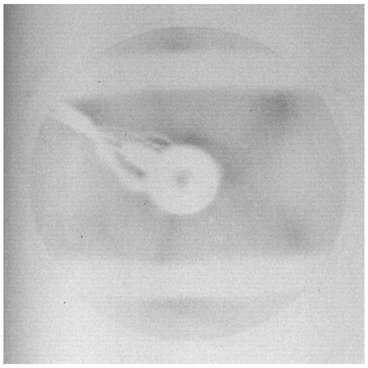

(c) 84.2 eV, 10 ML, 10^{-6} Torr, 1050 L, 3.0 ± 0.1Å

Figure 4.11: *LEED images for reactive growth of ultrathin CoO/Co/W(110) films. The incident beam energy, the equivalent Co film thickness,* O_2 *pressure, and the hexagonal lattice spacing are provided below each image. All samples were grown on a 10 ML Co/W(110) film. In a), reciprocal lattice vectors used to determine lattice spacing are drawn.*

trinsically disordered due to grain boundaries between islands, resulting in a diffuse LEED pattern much like the patterns in figures 4.10 and 4.11. Susceptibility measurements of AFM/FM bilayers are dependent on the size of the islands or grains as the grain size affects T_N and the strength of interfacial exchange interaction (see section 2.6.1). Specific heat measurements of ultrathin CoO/SiN_x films by Molina-Ruiz *et. al* [9] found that T_N increases with grain size and is thus indirectly related to film thickness. Changes in the intensity of the LEED spots can be attributed to different filament temperatures (hotter filaments emit more electrons).

The inter-planar spacing for ultrathin CoO/Co/W(110) films is found using the beam energies that correspond to LEED intensity maxima, as described in section 3.4. Figure 4.12(a) (4.12(b)) plots the LEED intensity maxima energies *versus* O_2 exposure (O_2 pressure) for exposure (reactive) growth samples. On the left side of each graph, the resonant energies of Co are listed. In figure 4.12(a) the resonant energies of the 500 L and 5000 L sample are identical, indicating that the structure within the probing depth of LEED has the same inter-planar spacing for both samples. The 5 L sample has an intermediate set of resonance energies; therefore, the structure changes within the LEED probing depth. Matsuyama and Ignatiev's [46] work on the oxidation of the Co(0001) plane found that exposures greater than 150 L are required to observe an ordered CoO structure, which is consistent with these results. In figure 4.12(b) no intermediate structure is observed for reactive growth samples.

All O_2 pressures correspond to the same set of resonant energies, even for pressures as low as 10^{-9} Torr. This is unreasonable as the number of O atoms that would come into contact with Co atoms at this pressure is much less than that needed to create a film composed of equal amounts of Co and O. Sindhu *et. al* [39] found that a minimum pressure of 10^{-4} Pa (7.5×10^{-7} Torr) is needed to produce CoO films *via* reactive growth on a Au (111) substrate. As stated above, there is additional O present that desorbs from the surfaces of the evaporator, which likely contributes to the lack of intermediate structure. The amount of O that will desorb from the evaporator is small compared to the ambient O present for pressures of 10^{-7} Torr and 10^{-6} Torr.

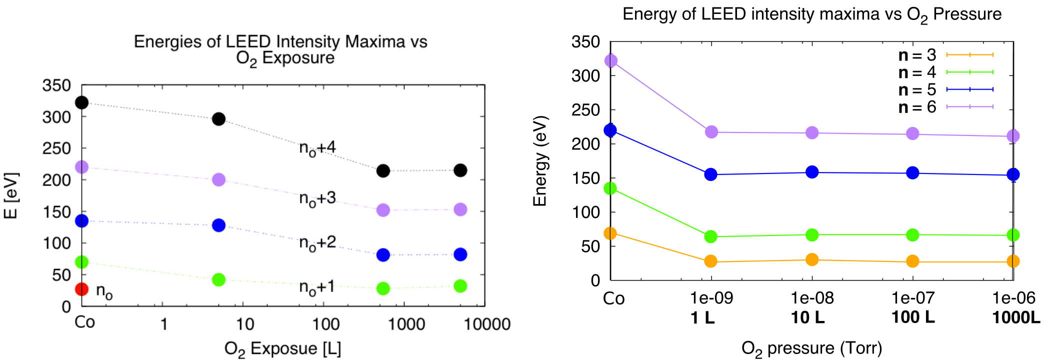

(a) Exposure growth

(b) Reactive growth

Figure 4.12: *Plot of resonant energies of the central LEED spot* versus*: a) exposure to O_2; b) O_2 pressure during growth. Lines are drawn connecting points of equal diffraction order. In b), the O_2 exposure during a 10 ML growth is given below the pressure.*

The determination of n_o and justification for assigning a different diffraction order to the first observed resonant energies of the oxidized and unoxidized films come from linearly fitting the energies to the diffraction order squared. All fits should have an intercept between -10 and -25 eV as this is the range of intercepts given by the linear fits for the inter-planar spacing of the W(110) substrate and Co films (these spacings could be definitively determined by fitting alone). Determining n_o based solely on the best fit of the slope cannot be done in some cases because the fit is dependent on n^2. As n increases the distance between points on the n^2 axis increase quadratically so that the fit will be better for higher n_o; for the extreme case of $n_o = \infty$ a horizontal line gives a perfect fit. It is wise then to compare the resonant energies to an expected set of resonant energies to see what value of n_o is reasonable. For oxidized Co films the expected energies of bulk Co and CoO will be used for comparison as the bulk Co spacings were found for Co films. The effect of the oxidization could just be a surface effect; if so, the inter-planar spacing would resemble that of Co. Figure 4.13 shows the variance between the measured resonant energies of an oxidized Co film and the expected resonant energies of bulk Co and CoO. The bulk Co energies are best fit for $n_o = 2$ and the bulk CoO energies are best fit for $n_o = 3$. An offset that is determined by fitting the energies to the expected bulk result is removed from the data so that any experimental offset does not contribute to the variance.

From figure 4.13 it can be seen that the variance is smallest for a CoO

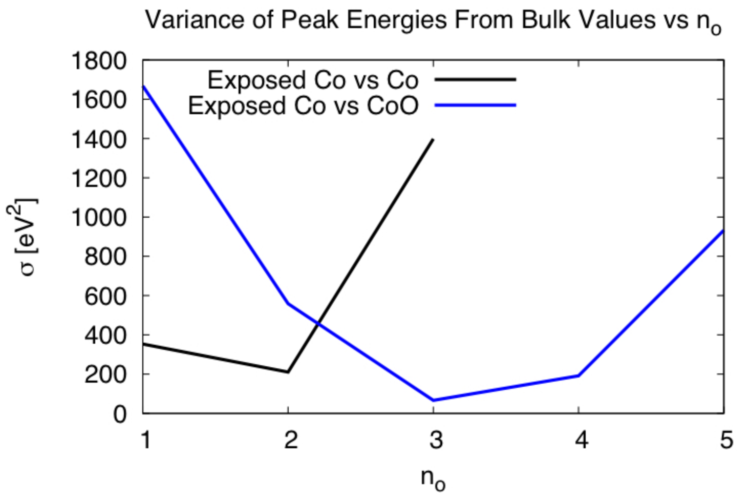

Figure 4.13: *Plot of variance between expected bulk and measured resonance energies* versus n_o *for an oxidized Co film. The black (blue) line is the variance with respect to the Co (CoO) resonant energies.*

spacing with $n_o = 3$. Table 4.3 lists n_o values with: variance; intercept energy, E_{int}, from the linear fit of the resonant energies *versus* diffraction order squared graph (E *versus* n^2); and the inter-planar spacing derived from the E *versus* n^2 graph. For W and Co samples the variance is small and the choice in n_o is obvious; however, the variance of W is higher as greater energy intensity peaks were used. Of reasonable n_o values, $n_o = 2$ for Co corresponds to the best fit of the E *versus* n^2 graph. The W and Co samples set the range of expected values of E_{int} as their value of n_o can be confidently determined from the known lattice spacing in the case of W and from the line of best fit for Co. For the exposed samples, the minimum in variance occurs when $n_o = 3$ in the

CoO lattice model, which has an E_{int} that coincides within the range specified by the W and Co samples. The level of confidence in the model is determined using the f ratio of the variances. There is a 91% confidence level in the CoO $n_o = 3$ model over the Co $n_o = 2$ model and a 89% confidence level over the CoO $n_o = 4$ model. For the reactive growth samples the variance is minimized for the CoO $n_o = 4$ model; although the variance is similar to that of the CoO $n_o = 3$ model. There is a 57% confidence level in the CoO $n_o = 4$ model over the CoO $n_o = 3$ model and a 86% confidence level over the Co $n_o = 2$ model. The E_{int} range set by the W and Co samples is best fit by $n_o = 3$, making this model the best choice. From this evidence, it can be concluded that the first observed intensity maxima for exposure and reactive growth samples are labelled as $n_o = 3$ and that the CoO layer extends past the surface.

Figures 4.14(a) and 4.14(b) are the E *versus* n^2 plots for a 5000 L exposure growth sample and a 10 ML reactive growth sample at a partial O_2 pressure of 10^{-7} Torr, respectively. The slope of the graph is used to find the inter-planar spacing with equation 3.17. The spacing for these particular exposure growth and reactive growth samples are 2.37 ± 0.04 Å and 2.26 ± 0.08 Å, respectively. Some variation from bulk values is reasonable in strained ultrathin samples. Table 4.4 shows that the average inter-planar spacing of many exposure growth films match the bulk spacing, while the average of many reactive growth films is slightly smaller. The average in-plane and inter-planar spacing of multiple samples is listed in table 4.4, with bulk values for CoO and Co_3O_4. Co_3O_4 is

Sample	Model	n_o	σ [eV^2]	E_{int} [eV]	d [Å]
W(110)	W	5	7.4	-22 ± 3eV	2.23 ± 0.07
Co 10 ML	Co	2	4.1	-11 ± 1eV	2.01 ± 0.01
Co 10 ML	Co	2	210	6 ± 6	2.13 ± 0.05
+	CoO	3	66	-24 ± 5	2.37 ± 0.04
5000 L O_2	CoO	4	190	-55 ± 5	2.60 ± 0.07
Co 10 ML	Co	2	693	5 ± 9	2.16 ± 0.03
at 10^{-6} Torr O^2	CoO	3	257	-30 ± 7	2.36 ± 0.03
+ 1050 L O_2	CoO	4	214	-68 ± 7	2.54 ± 0.03

Table 4.3: *Comparison of measured and expected resonance energies. The second column is the model lattice used to find the expected energies. n_o is the order of the first observed peak; σ is the variance; E_{int} is the intercept energy of the E* versus *n^2 graph; d is the inter-planar spacing.*

another common oxide of Co that also has hexagonal lattice structure in the (111) plane, but with a much larger lattice spacing [72]. The two structures share a common fcc O sublattice that only differs in size by $\sim 5\%$ [73]. It is also AFM but has a much lower Néel temperature of 40 K [74], which is below the temperature range of our system and is thus unwanted. The LEED analysis clearly shows that CoO is being formed instead of Co_3O_4. Both exposure and reactive growth methods produce CoO films of thicknesses greater than the probing depth of LEED. As stated in section 3.5.2, exposure growth films are favoured as exposed films create the greatest interfacial exchange interaction and the process of reactive growth compromises the purity of subsequent Co film growth.

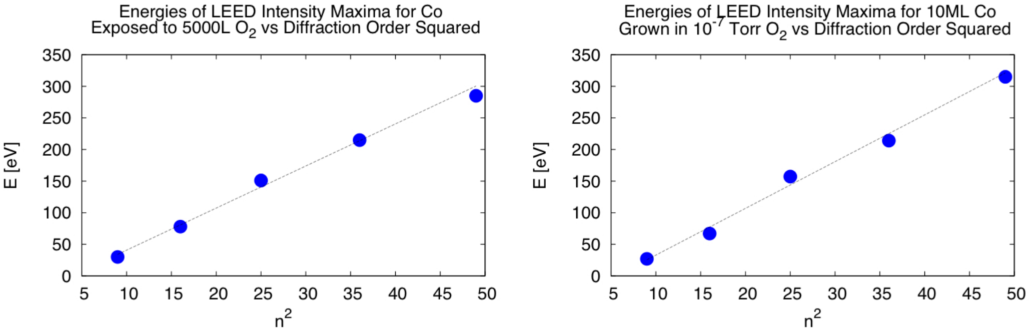

(a) Exposure growth

(b) Reactive growth

Figure 4.14: *Plots of resonant energies of the central LEED spot* versus *diffraction order squared for ultrathin CoO/Co/W(110) films. Using equation 3.17 the slope gives inter-planar spacings of a)* 2.37 ± 0.04 $\mathring{A}$ *and b)* 2.26 ± 0.08 $\mathring{A}$.

4.2.3 Transverse susceptibility of ultrathin CoO/Co/W(110) films

The three samples of Co/W(110) used to find the in-plane anisotropy (A, B, and C) were subsequently exposed to 5000 L (A and B) or 10,000 L (C) of O_2 to produce ultrathin CoO/Co/W(110) films. These exposures nearly saturate the film, so the oxide layer is expected to be 10-25 nm thick [41, 47, 51, 55].

Lattice parameter	Exposure growth	Reactive growth	CoO bulk	Co_3O_4 bulk
a_{hex}: In-plane hexangonal lattice spacing [Å]	3.0 ± 0.1	3.0 ± 0.1	3.012	5.716
d: Inter-planar spacing [Å]	2.41 ± 0.09	2.31 ± 0.05	2.459	4.667

Table 4.4: *Inter-planar spacings and in-plane lattice spacings for exposure and reactive growth of ultrathin CoO films, bulk CoO, and bulk Co_3O_4.*

Exposure growth was used because it prevented the evaporator from absorbing oxygen that spoils the purity of subsequent Co films. Transverse susceptibility measurements of ultrathin CoO/Co/W(110) films were performed on all three samples over a large temperature range to find evidence of the Néel transition *via* the interfacial exchange interaction between the AFM CoO and the FM Co layers. The lower limit of the temperature range was $\sim$ 150 K due to the limitation of our cooling system; however, this is sufficiently cool as it has been shown that *hcp* Co (0001) forms Co_3O_4 when oxidized at 120 K [51], and that 150 K is below previously reported Néel temperatures for films greater than 1 nm [75]. The upper temperature limit is selected to be $\sim$ 320 K as this is well over the bulk Néel temperature of 290 K.

The transverse susceptibility of the CoO/Co/W(110) samples is shown in figure 4.15 along with the real part of the parent Co film's transverse susceptibility, except in (b), which is a close-up of sample A's susceptibility. The difference in susceptibility at room temperature (above T_N) is likely caused by the consumption of the FM layer by oxidation in order to create the AFM layer. This difference is largest in sample A where the susceptibility of the film after exposure drops to a quarter of its initial value. In samples B and C the change in susceptibility over the entire temperature range is obviously greater for the oxidized film compared to the parent film – this is also true for sample A. The disparity between the transverse susceptibility of the ultrathin CoO/Co/W(110) and Co/W(110) films increases at lower temperatures as the AFM layer of the ultrathin CoO/Co/W(110) film will become ordered below T_N, contributing an additional term to the anisotropy through the interfacial exchange interaction. In all three samples, a broad hump in the real part of the transverse susceptibility curve occurs near 200 K. The rate at which the susceptibility rises with increasing temperature is greater at temperatures below this hump than above it, corresponding to temperatures below and above T_N. In samples B and C there is clearly a broad peak in the imaginary susceptibility curve that has a similar width and temperature range as the hump in the real part of the susceptibility. Sample A gives a hint of such a feature, but it is uncertain. This imaginary peak indicates energy is being absorbed by the system, corresponding to an increase in the degrees of freedom of the magnetic moments in the Co layer as the constraint imposed on the transverse susceptibility by the interfacial exchange interaction vanishes during the Néel transition. At temperatures below (above) T_N, the magnetic moments are frozen in place (move freely); therefore, energy is not dissipated into the system. At T_N the magnetic moments respond sluggishly when they become unfrozen. This is analogous to mechanical friction in that motion is slowed by dissipating energy into the system. The peaks are broad, which is to be expected of a rough polycrystalline sample as previous studies have shown that T_N is strongly related to crystallite size and film thickness [75, 76]. These features in the transverse susceptibility are definite signs of the Néel transition.

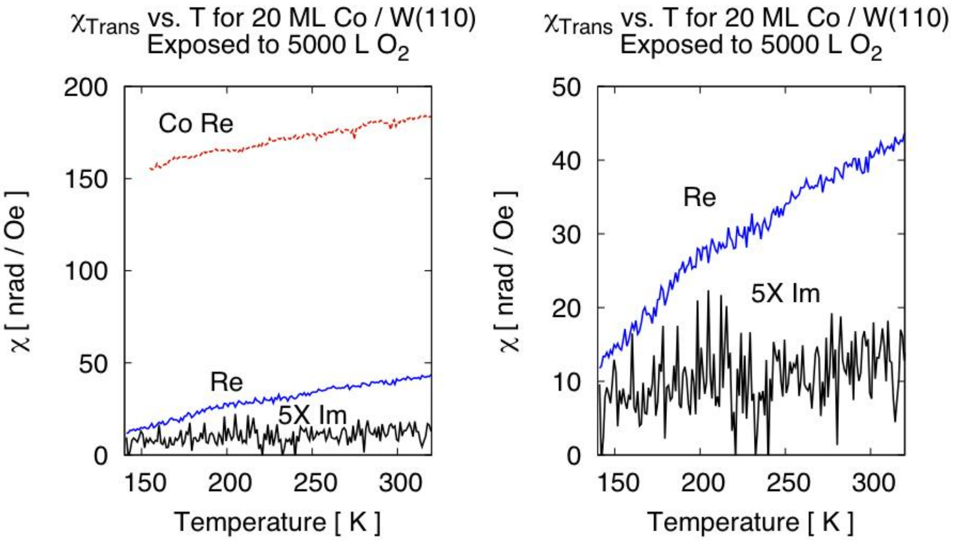

(a) Sample A (b) Sample A

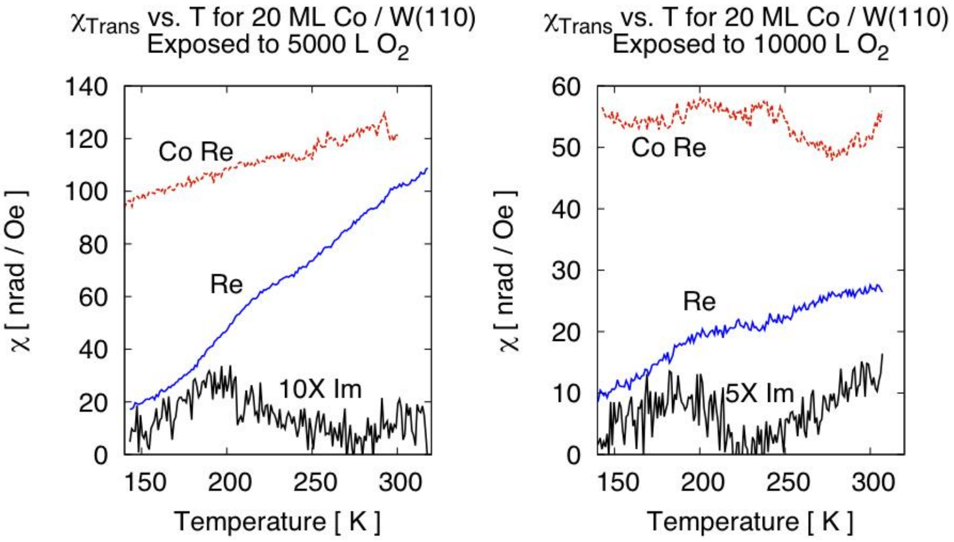

(c) Sample B (d) Sample C

Figure 4.15: *Plots of transverse susceptibility of ultrathin CoO/Co/W(110) films* versus *temperature. The real part of the transverse susceptibility of the parent Co film is shown in a), c), and d); b) is a close-up of a).*

Chapter 5

Conclusion

5.1 Anisotropy of ultrathin Co/W(110) films

This study performed *in situ* measurements of the in-plane magnetic anisotropy of ultrathin Co/W(110) films using SMOKE. Ultrathin Co/W(110) films were first grown and characterized by AES and LEED, which clearly showed a well ordered Co (0001) film. Next, the ability of the SMOKE apparatus to measure the transverse magnetic susceptibility of an ultrathin Co/W(110) film was tested. Experiments were subsequently performed to ensure a linear magnetic response from the film to an applied field. Background noise obscuring the signal was diminished five-fold by isolating components of the apparatus in order to prevent a ground loop. Once the noise was removed, susceptibility measurement sensitivities of $\sim 1\ \frac{\text{nrad}}{\text{Oe}}$ (~ 10 nrad absolute) were achieved and the magnetization was found to vary linearly with field. Magnetic hysteresis and susceptibility measurements were made to determine the in-plane magnetic anisotropy.

The magnetic hysteresis loops provide a measure of the Kerr rotation of the saturated magnetization of 10 ML and 20 ML Co/W(110) films. The Kerr rotation per monolayer for a saturated film was found to be $2.0 \pm 0.5 \ \frac{\mu\text{rad}}{\text{ML}}$ for a 10 ML sample and $0.9 \pm 0.1 \ \frac{\mu\text{rad}}{\text{ML}}$ for a 20 ML sample. As both of the samples fall in the incoherent thickness regime, where the anisotropy is not linear with thickness, these values of the Kerr rotation are lower than what is expected for thinner films within the coherent regime. Even with this consideration, these values seem low in comparison to results obtained for the saturated Kerr rotation per monolayer for ultrathin Co/Cu(001) and Co/Cu(1117) films by Oepen *et. al* [69, 70], which were an order of magnitude greater. The square shape of the hysteresis loops indicates that domain wall motion is responsible for the change in magnetization. It is possible that the magnetization only changed in a fraction of the entire probing area, thus producing a smaller signal. This would be caused by pinning of domain walls, which inhibits spin reversal. The discrepancy between the 10 ML and 20 ML films and the large number of samples where a hysteresis loop was not obtained could also be attributed to partial or complete pinning in the probed area. More dc measurements with larger fields are required to confirm the reported value of the saturated Kerr rotation per monolayer.

The transverse susceptibility was successfully measured for three samples over a large range of temperatures. Although they differed in magnitude, samples A and B showed the expected linear dependency of the transverse susceptibility on the temperature, with similar slopes of $0.162 \pm 0.002\ \frac{\text{nrad}}{\text{Oe K}}$ and $0.196 \pm 0.002\ \frac{\text{nrad}}{\text{Oe K}}$. Samples A and C showed the expected small featureless imaginary components. The inconsistencies in these measurements have been attributed to varying amounts of contaminants in the system. A thorough cleaning of the evaporator and a larger sample population is necessary to accurately determine the transverse susceptibility.

The transverse magnetic anisotropy was successfully calculated from the quotient of the saturation Kerr rotation of the film and the transverse susceptibility, which were both measured *in situ* by SMOKE. The results were a factor of eight lower than estimates by Fritzsche *et. al* [1]. This is reasonable considering the inconsistencies in the magnetic saturation and transverse susceptibility measurements. In order to verify the results of this work, a study with more samples, a clean evaporator, and a larger field is required. Beyond this, a more complete set of film thicknesses would provide a better comparison to the work by Fritzsche *et. al* [1].

5.2 Néel transition in ultrathin CoO/Co/W(110) films

Observing the *in situ* Néel transition in AFM ultrathin films is a daunting task because of the zero net magnetization and minute sample size; nonetheless, this was achieved by SMOKE measurements of the transverse susceptibility of a coupled AFM/FM bilayer film. CoO/Co/W(110) bilayers created the choice system of study by providing a strong interfacial exchange interaction and an in-plane easy axis. AES and LEED studies were used to determine the successful growth of ultrathin CoO/Co/W(110) films by reactive and exposure growth methods. The exposure growth method is preferred because it creates the greatest interfacial exchange interaction and due to the fact that reactive growth compromises the purity of subsequent Co film growth. The hexagonal LEED pattern marks the presence of the (111) plane of CoO, which is desired as this surface should maximize the interfacial exchange interaction.

Transverse susceptibility measurements show that all samples have overall decreases in susceptibility compared to the corresponding parent films due in part to consumption of the FM Co layer to form the AFM CoO layer. The real part of the susceptibility increases monotonically with temperature by a rate greater than that of the parent Co films. The greater slope may be caused by changes to the band structure and/or additional anisotropy of the interfacial exchange interaction. The magnitudes of the slope and the susceptibility of the three samples vary, but this is expected as the transverse susceptibility of the parent films differed. A broad hump in the real part of the transverse susceptibility at 200 K accompanied by a change in slope on either side occurs in all samples. A matching hump at the same temperature has been observed in the imaginary susceptibility of samples B, C, and possibly A. The coincidence of these peeks is a clear indication of the Néel transition. The real peak corresponds to the reorientation of magnetic moments and the imaginary peak corresponds to an increase in the degrees of freedom of the magnetic moments. The polycrystalline film produces a broad peak as T_N is sensitive to grain size. The Néel transition of an *in situ* AFM ultrathin CoO/Co/W(110) film has been observed and T_N was found to be around 200 K.

The results for T_N in this experiment were surprisingly consistent, despite the variation in the transverse susceptibility. Having parent Co/W(110) films with consistent magnetic properties would allow for more information to be obtained from these experiments. Hysteresis measurements would be helpful in determining what affect the CoO layer had on the anisotropy of the Co layer. Lesser oxygen exposures would allow a study of the Néel transition *versus* oxide thickness.

Bibliography

[1] Fritzsche, H., Kohlhepp, J., and Gradmann, U. Epitaxial strain and magnetic anisotropy in ultrathin Co films on W(110). *Phys. Rev. B* **51**(22), 15933–15941 (1995).

[2] Heinrich, B. and Bland, J. A. C. Introduction. In *Ultrathin magnetic structures vol. I.,* Bland, J. A. C. and Heinrich, B., editors, 1–6. Springer-Verlag (2005).

[3] de Jonge, W. J. M., Bloemen, P. J. H., and den Broeder, F. J. A. Experimental investigations of magnetic anisotropy. In *Ultrathin magnetic structures vol. I.,* Bland, J. A. C. and Heinrich, B., editors, 65–86. Springer-Verlag (2005).

[4] Duden, T. and Bauer, E. Spin-polarized low energy electron microscopy of ferromagnetic layers. *J. Electron Microsc.* **47**(5), 379–385 (1998).

[5] Fert, A. and Bruno, P. Interlayer coupling and magnetoresistance in multilayers. In *Ultrathin magnetic structures vol. II.,* Heinrich, B. and

Bland, J. A. C., editors, 82–117. Springer-Verlag (2005).

[6] Heinrich, B. Ferromagnetic resonance in ultrathin film structures. In *Ultrathin magnetic structures vol. II.,* Heinrich, B. and Bland, J. A. C., editors, 195–222. Springer-Verlag (2005).

[7] Cochran, J. F. Light scattering from ultrathin magnetic layers and bilayers. In *Ultrathin magnetic structures vol. II.,* Heinrich, B. and Bland, J. A. C., editors, 222–257. Springer-Verlag (2005).

[8] Nobelprize.org. Louis Néel - biography. url : http://www.nobelprize.org/nobel_prizes/physics/laureates/1970/neel-bio.html, July (2012).

[9] Molina-Ruiz, M., Lopeandía, A. F., Pi, F., Givord, D., Bourgeois, O., and Rodríguez-Viejo, J. Evidence of finite-size effect on the Néel temperature in ultrathin layers of CoO nanograins. *Phys. Rev. B* **83**(140407(R)), 1–4 (2011).

[10] Arrott, A. S. Magnetism in SI units and Gaussian units. In *Ultrathin magnetic structures vol. I.,* Bland, J. A. C. and Heinrich, B., editors, 7–19. Springer-Verlag (2005).

[11] Venus, D., Arnold, C. S., and Dunlavy, M. Domains in perpendicularly magnetized ultrathin films studied using the magnetic susceptibility. *Phys. Rev. B* **60**(13), 9607–9615 (1999).

[12] Osbourn, J. A. Demagnetizing factors of the general ellipsoid. *Phys. Rev.* **67**(11-12), 351–357 (1945).

[13] Néel, L. Anisotropie magnétique superficielle et surstructures d'orientation. *J. de Phys. et le Rad.* **15**(4), 225–239 (1954).

[14] Johnson, M. T., Bloemen, P. J. H., den Broeder, F. J. A., and de Vries, J. J. Magnetic anisotropy in metallic multilayers. *Rep. Prog. Phys.* **59**, 1409–1458 (1996).

[15] Mills, D. L. Thermodynamic properties of ultrathin ferromagnetic films. In *Ultrathin magnetic structures vol. I.,* Bland, J. A. C. and Heinrich, B., editors, 91–121. Springer-Verlag (2005).

[16] Poulopoulos, P. and Baberschke, K. Magnetism in thin films. *J. Phys.: Condens. Matter* **11**, 9495–9515 (1999).

[17] Chikazumi, S. *Physics of ferromagnetism* 2^{nd} *Ed.* Clarendon Press, (1997).

[18] Csiszar, S. I., Haverkort, M. W., Hu, Z., Tanaka, A., Hsieh, H. H., Lin, H.-J., Chen, C. T., Hibma, T., and Tjeng, L. H. Controlling orbital moment and spin orientation in CoO layers by strain. *PRL* **95**(187205), 1–4 (2005).

[19] Heinrich, B. and Cochran, J. F. Ultrathin metallic magnetic films: magnetic anisotropies and exchange interactions. *Adv. Phys.* **42**(5), 523–639 (1993).

[20] Sucksmith, W. and Thompson, J. E. The magnetic anisotropy of cobalt. *Proc. R. Soc. London, Ser. A* **225**(1162), 362–375 (1954).

[21] Betteridge, W. The properties of metallic cobalt. *Prog. Mat. Sci.* **24**, 51–142 (1979).

[22] Bruno, P. Magnetic surface anisotropy of cobalt and surface roughness effects within Néel's model. *J. Phys. F: Met. Phys.* **18**, 1291–1298 (1988).

[23] Pinkvos, H., Poppa, H., Bauer, E., and Hurst, J. Spin-polarized low-energy electron microscopy study of the magnetic microstructure of ultrathin epitaxial cobalt films on W(110). *Ultramicroscopy* **47**, 339–345 (1992).

[24] Bansmann, J., Lu, L., Getzlaff, M., and Meiwes-Broer, K. H. Magnetic properties of transition metal films and islands on W(110). *Z. Phys. D* **40**, 570–573 (1997).

[25] Ociepa, J. G., Schultz, P. J., Griffiths, K., and Norton, P. R. Re-emitted positron energy spectroscopy from thin Co films on W(110). *Surf. Sci.* **225**, 281–291 (1990).

[26] Alberts, L. and Alberts, H. L. The magnetostriction of polycrystalline cobalt. *Phil. Mag.* **8**(96), 2101–2102 (1963).

[27] Kleibert, A., Senz, V., Bansmann, J., and Oppeneer, P. M. Thickness dependence and magnetocrystalline anisotropy of the x-ray transverse magneto-optical Kerr effect at the Co $2p$ edges of ultrathin Co films on W(110). *Phys. Rev. B* **72**(144404), 1–10 (2005).

[28] Meiklejohn, W. H. and Bean, C. P. New magnetic anisotropy. *Phys. Rev.* **105**(3), 903–914 (1956).

[29] Berkowitz, A. E. and Takano, K. Exchange anisotropy - a review. *J. Magn. Magn. Mater.* **200**, 552–570 (1999).

[30] Nogués, J. and Schuller, I. K. Exchange bias. *J. Magn. Magn. Mater.* **192**, 203–232 (1999).

[31] Jauch, W., Reehuis, M., Bleif, H. J., Kubanek, F., and Pattison, P. Crystallographic symmetry and magnetic structure of CoO. *Phys. Rev. B* **64**(052102), 1–3 (2001).

[32] Shull, C. G., Strauser, W. A., and Wollan, E. O. Neutron Diffraction by Paramagnetic and Antiferromagnetic Substances. *Phys. Rev.* **83**(2), 333–345 (1951).

[33] Roth, W. L. Magnetic structure of MnO, FeO, CoO and NiO. *Phys. Rev.* **110**(6), 1333–1341 (1958).

[34] van Laar, B. Multi-spin-axis structure for CoO. *Phys. Rev.* **138**(2A), A 584–A 587 (1965).

[35] Herrmann-Ronzaud, D., Burlet, P., and Rossat-Mignod, J. Equivalent type-II magnetic structures: CoO, a collinear antiferromagnet. *J. Phys. C: Solid State Phys.* **11**, 2123–2137 (1978).

[36] Tomiyasu, K., Inami, T., and Ikeda, N. Magnetic structure of CoO studied by neutron and synchrotron x-ray diffraction. *Phys. Rev. B* **70**(184411), 1–6 (2004).

[37] Ressouche, E., Kernavanois, N., Regnault, L.-P., and Henry, J.-Y. Magnetic structures of the metal monoxides NiO and CoO re-investigated by spherical neutron polarimetry. *Physica B* **385-386**, 394–397 (2006).

[38] Bridge, M. E. and Lambert, R. M. Oxygen chemisorption, surface oxidation, and the oxidation of carbon monoxide on cobalt (0001). *Surf. Sci.* **82**, 413–424 (1979).

[39] Sindhu, S., Heiler, M., Schindler, K.-M., and Neddermeyer, H. A photoemission study of CoO-films on Au(111). *Surf. Sci.* **514**, 197–206 (2003).

[40] Garreau, G., Farle, M., Beaurepaire, E., and Bakerschke, K. Curie temperature and morphology in ultrathin Co/W(110) films. *Phys. Rev. B* **55**(1), 330–335 (1997).

[41] Gruyters, M. Structural and magnetic properties of transition metals oxide/metal bilayers prepared by *in situ* oxidation. *J. Magn. Magn. Mater.* **248**, 248–257 (2002).

[42] Bettac, A., Bansmann, J., Senz, V., and Meiwes-Broer, K. H. Structure and magnetism of hcp(0001) and fcc (001) thin cobalt films on a clean and carbon-reconstructed W(110) surface. *Surf. Sci.* **454-456**, 936–941 (2000).

[43] Jones, T. L. A structural and magnetic characterization of ultrathin iron films on a W(100) substrate. Master's thesis, McMaster University, Hamilton, Ontario, (1993).

[44] Childs, K. D. and Hedberg, C. L. *Handbook of Auger electron spectroscopy: a book of reference data for identification and interpretation in Auger electron spectrscopy* 3^{rd} *Ed.* Physical electronic Inc, (1995).

[45] Cool, S. C. Spin-polarized low energy electron diffraction rotation curves used to investigate ultrathin magnetic films: iron on a tungsten (110) substrate. Master's thesis, McMaster University, Hamilton, Ontario, (1997).

[46] Matsuyama, T. and Ignatiev, A. LEED-AES study of the temperature dependent oxidation of the cobalt (0001) surface. *Surf. Sci.* **102**, 18–21 (1981).

[47] Duò, L., Finazzi, M., Ciccacci, F., and Braicovich, L. Interaction of oxygen with polycrystalline cobalt studied by inverse-photoemission spectroscopy. *Phys. Rev. B* **47**(23), 15848–15851 (1993).

[48] Clemens, W., Vescovo, E., Kachel, T., Carbone, C., and Eberhardt, W. Spin-resolved photoemission study of the reaction of O_2 with fcc Co(100). *Phys. Rev. B* **46**(7), 4198–4204 (1992).

[49] Klingenberg, B., Grellner, F., Borgmann, D., and Welder, G. Low-energy electron diffraction and X-ray photoelectron spectroscopy on the oxidation of cobalt $(11\bar{2}0)$. *Surf. Sci.* **383**, 13–24 (1997).

[50] Brundle, C. R., Chaung, T. J., and Rice, D. W. X-ray photoemission study of the interaction of oxygen and air with clean cobalt surfaces. *Surf. Sci.* **60**(2), 286–300 (1976).

[51] Castro, G. R. and Küppers, J. Interaction of oxygen with hcp (0001) recrystallized cobalt surfaces. *Surf. Sci.* **123**(2-3), 456–470 (1982).

[52] Getzlaff, M., Bansmann, J., and Schönhense, G. Magnetic interactions in different oxidation states of thin cobalt films. *J. Magn. Magn. Mater.* **131**(3), 304–310 (1994).

[53] Gruyters, M. and Riegel, D. Optimized exchange biasing by controlled *in situ* oxidation. *J. Appl. Phys.* **88**(11), 6610 – 6613 (2000).

[54] Getzlaff, M., Bansann, J., and Schönhense, G. Spin resolved photoemission study of oxygen on thin cobalt films. *J. Electron. Spectrosc. Relat. Phenom.* **77**(2), 197–207 (1996).

[55] Smardz, L., Köbler, U., and Zinn, W. Oxidation kinetics of thin and ultrathin cobalt films. *J. Appl. Phys.* **71**(10), 5199–5204 (1992).

[56] Schindler, K.-M., Wang, J., Chassé, A., Neddermeyer, H., and Widdra, W. Low-energy electron diffraction structure determination of an ultrathin CoO film on Ag(001). *Surf. Sci.* **603**, 2658–2663 (2009).

[57] Torelli, P., Soares, E. A., Renaud, G., Valeri, S., Guo, X. X., and Luches, P. Nano-structuration of CoO film by misfit dislocations. *Surf. Sci.* **601**, 2651–2655 (2007).

[58] Zak, J., Moog, E. R., Liu, C., and Bader, S. D. Universal approach to magneto-optics. *J. Magn. Magn. Mater.* **89**, 107–123 (1990).

[59] Dunlavy, M. J. *Static and dynamic critical phenomena in ultrathin films of iron on W(110).* PhD thesis, McMaster University, Hamilton, Ontario, (2003).

[60] Zak, J., Moog, E. R., Liu, C., and Bader, S. D. Magneto-optics of multilayers with arbitrary magnetization directions. *Phys. Rev. B* **43**(8), 6423–6429 (1991).

[61] Bader, S. D. and Erskine, J. L. Magneto-optical effects in ultrathin magnetic structures. In *Ultrathin magnetic structures vol. II.,* Heinrich, B. and Bland, J. A. C., editors, 297–325. Springer-Verlag (2005).

[62] Brubaker, M. E., Moog, E. R., Sowers, C. H., Zak, J., and Baber, S. D. Transverse magneto optic Kerr effect in ultrathin films. *J. Magn. Magn. Mater.* **103**(1-2), L7–L12 (1992).

[63] Arnold, C. S. and Venus, D. Simple window-compensation method for improving the signal-to-noise ratio in measurements of the magneto-optic Kerr effect in ultrathin films. *Rev. Sci. Instrum.* **66**(5), 3280–3283 (1995).

[64] Arnold, C. S. Magnetic susceptibility measurements of ultrathin films using the surface magneto-optic Kerr effect: Optimization of the signal-to-noise ratio. *Rev. Sci. Instrum.* **68**(11), 4212–4216 (1997).

[65] Fritsch, K. Optimization of magnetic susceptibility measurements on ultrathin films. Master's thesis, McMaster University, Hamilton, Ontario, (2008).

[66] Pratzer, M. and Elmers, H. J. Structure and electronic properties of ultrathin Co films on W(110). *Surf. Sci.* **550**, 223–232 (2004).

[67] Pratzer, M. and Elmers, H. J. Scanning tunneling spectroscopy of dislocations in ultrathin *fcc* and *hcp* Co films. *Phys. Rev. B* **72**(035460), 1–8 (2005).

[68] Johnson, B. G., Berlowitz, P. J., Goodman, D. W., and Bartholomew, C. H. The structural and chemisorptive properties of ultrathin cobalt overlayers on W(110) and W(100). *Surf. Sci.* **217**, 13–37 (1989).

[69] Berger, A., Knappmann, S., and Oepen, H. P. Magneto-optical Kerr effect study of ac susceptibilities in ultrathin cobalt films. *J. Appl. Phys.* **75**(10), 5598–5600 (1994).

[70] Oepen, H. P., Knappmann, S., and Wulfhekel, W. Ferro- and paramagnetic properties of ultrathin epitaxial Co/Cu films. *J. Magn. Magn. Mater.* **148**, 90–92 (1995).

[71] Lee, B. W., Ignatiev, A., Taylor, J. A., and Rabalais, J. W. Atomic structure sensitivity of XPS: the oxidation of cobalt. *Solid State Commun.* **33**(12), 1205–1208 (1980).

[72] Meyer, W., Biedermann, K., Gubo, M., Hammer, L., and Heinz, K. Surface structure of polar Co_3O_4(111) films grown epitaxially on Ir(100)-(1x1). *J. Phys.: Condens. Matter* **20**(265011), 1–6 (2008).

[73] Petitto, S. C., Marsh, E. M., Carson, G. A., and Langell, M. A. Cobalt oxide surface chemistry: The interaction of CoO(100), Co_3O_4(110) and Co_3O_4(111) with oxygen and water. *J. Mol. Catal. A: Chem.* **281**, 49–58 (2008).

[74] Roth, W. L. The magnetic structure of Co_3O_4. *J. Phys. Chem. Solids* **25**, 1–10 (1964).

[75] Venus, D. and Hunte, F. Competition between magnetic relaxation mechanisms in exchange-coupled CoO/Co bilayers. *Phys. Rev. B* **72**(024404), 1–14 (2005).

[76] Tang, Y. J., Smith, D. J., Zink, B. L., Hellman, F., and Berkowitz, A. E. Finite size effects on the moment and ordering temperature in antiferromagnetic CoO layers. *Phys. Rev. B* **67**(054408), 1–7 (2003).